Petroleum Science 20 (2023) 212–229

Contents lists available at ScienceDirect

Petroleum Science

journal homepage: www.keaipublishing.com/en/journals/petroleum-science

Original Paper

3D anisotropy in shear failure of a typical shale

Zi-Dong Fan [a, b], Li Ren [a, b, *], He-Ping Xie [a, c], Ru Zhang [a, d], Cun-Bao Li [a, c], Hui-Jun Lu [a, d], An-Lin Zhang [a, d], Qin Zhou [a, b], Wei-Qiang Ling [a, b]

[a] MOE Key Laboratory of Deep Earth Science and Engineering, Sichuan University, Chengdu, Sichuan 610065, China
[b] College of Architecture and Environment, Sichuan University, Chengdu, Sichuan 610065, China
[c] Institute of Deep Earth Sciences and Green Energy, Shenzhen University, Shenzhen, Guangdong 518052, China
[d] College of Water Resources and Hydropower, Sichuan University, Chengdu, Sichuan 610065, China

ARTICLE INFO

Article history:
Received 29 November 2021
Received in revised form
16 August 2022
Accepted 24 October 2022
Available online 30 October 2022

Edited by Jie Hao

Keywords:
Shale
Shear
Acoustic emission
Digital image correlation
X-ray computed tomography
Fracture network

ABSTRACT

It is inadequate to study the shear failure anisotropy of shale in only 2D space. Aiming at a 3D analysis, a series of direct shear tests was conducted on Longmaxi shale with three typical bedding orientations: arrester, divider and short-transverse orientations. During testing, acoustic emission (AE) and digital image correlation (DIC) techniques were simultaneously employed to monitor failure development, after testing, X-ray computed tomography (CT) scanning was adopted to acquire and reconstruct the fractures inside typical ruptured samples for more detailed analysis. The results indicated that the shear strength parameters exhibited 3D anisotropies and those of the arrester sample did not have equivalent shear strength parameters to the shale matrix. The maximum (minimum) shear strength and cohesion were obtained with the divider (short-transverse) orientation, and the internal friction angle reached its maximum (minimum) with the divider (arrester) orientation. Combining the AE, DIC and CT techniques, four characteristic stress levels that can capture the progressive shear failure process of shale rocks were identified, and the onset and accelerated development of shear damage-induced dilation were observed at the crack initiation and coalesce stress thresholds, respectively. During the crack coalescence stage, the dominated microcracking mechanism transferred from tensile-mode to shear-mode. For the arrester and divider orientations, more tensile-mode AE events were generated due to the microcracking along the vertical beddings. Compared with the divider samples, a more complex fracture network with a larger fracture area and volume was obtained in the arrester samples, whose strengths were smaller.

1. Introduction

Shale gas formations are reservoirs with critically low permeability, and both horizontal drilling and hydraulic fracturing techniques are, therefore, widely applied to enhance the production of shale gas (Arthur et al., 2009; Li et al., 2017). In previous studies, significant anisotropies have been observed in the mechanical properties of shale rocks (Cho et al., 2012; Fan et al., 2022a; He et al., 2021; Jin et al., 2018; Li et al., 2020; Masri et al., 2014; Ren et al., 2020), e.g., the elasticity, compressive strength and fracture propagation resistance. Meanwhile, studies have also shown that the shear failure of shale plays a dominant role in the wellbore instability and is one of the vital forms of crack propagation and coalescence during stimulated reservoir volume (SRV) treatments (Backers et al., 2012; McClure and Horne, 2014; Palmer et al., 2007). Thus, studying the anisotropic shear failure properties and mechanisms of shale has practical significance in improving the wellbore stability and stimulated efficiency of the reservoirs.

Shear failure is a main failure pattern in the uniaxial and triaxial compression tests of shale (Chen et al., 2021b; He et al., 2022; Hou et al., 2016; Lu et al., 2021a; Suo et al., 2020; Wang et al., 2016; Wang and Li, 2017), and it is clear that the shear failure pattern is significantly influenced by angle α between the axial loading direction and the normal to the bedding plane (Fig. 1a and b). In the uniaxial compression tests (UCTs), the failure patterns can be divided into three types (Chen et al., 2021b; Wang and Li, 2017): (1) when $\alpha = 0–15°$, the failure pattern is a combination of shear fractures and tensile fractures; (2) when $\alpha = 30–60°$, the failure is

* Corresponding author. MOE Key Laboratory of Deep Earth Science and Engineering, Sichuan University, Chengdu, Sichuan 610065, China.
E-mail addresses: renli-scu@hotmail.com, renli@scu.edu.cn (L. Ren).

https://doi.org/10.1016/j.petsci.2022.10.017

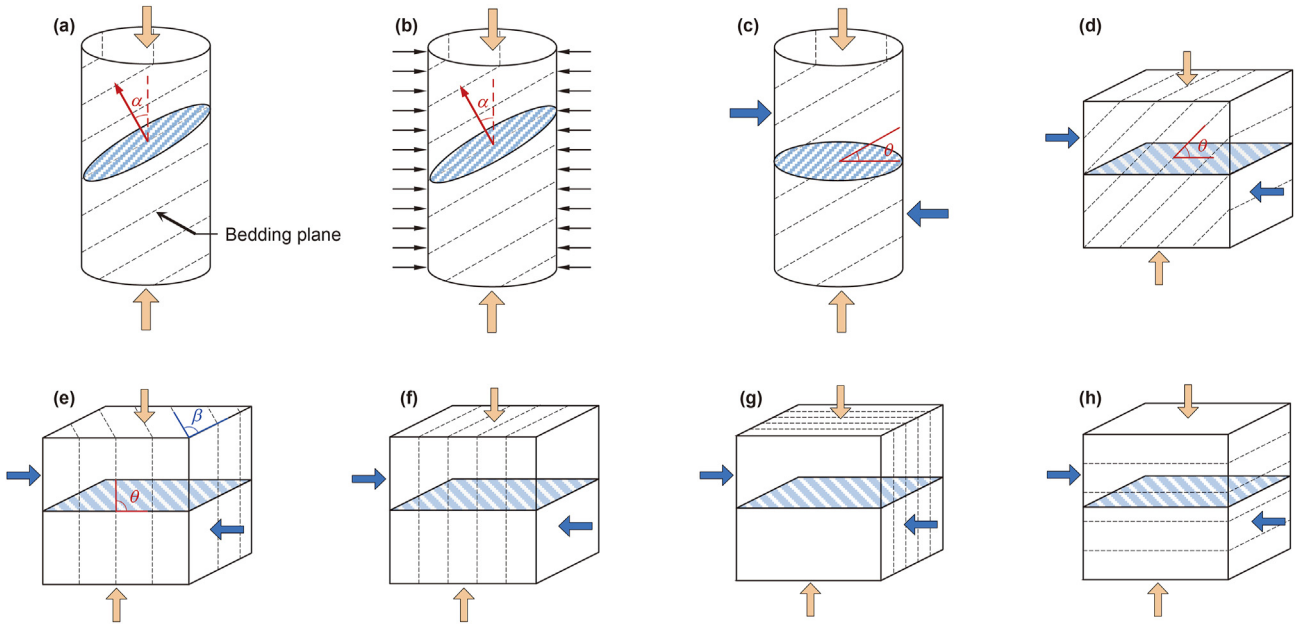

Fig. 1. Sketch of different experiments on shale. (a) Uniaxial compression test. (b) Triaxial compression test. (c) Direct shear test with a cylindrical sample. (d) Direct shear test with a cubic sample. (e) Definition of the bedding angle in 3D space. (f) Arrester sample. (g) Divider sample. (h) Short-transverse sample.

dominated by shear failure along or across the bedding planes; (3) when $\alpha = 75–90°$, tensile splitting failure along the beddings occurs. In the triaxial compression tests (TCTs), the high confining pressure compacts the bedding planes and restricts tensile cracks (Niandou et al., 1997; Wu et al., 2016; Yang et al., 2020). Accordingly, a single macroscopic shear fracture occurs for all bedding angles under the high confining pressure conditions. However, due to the limitations of uniaxial and triaxial compression tests, especially the uncertainty in locations of shear fracture surfaces (Heng et al., 2015), the anisotropies in the shear strength characteristics and failure mechanism of shale have not been clearly explained.

The direct shear experiment, which is considered an effective method to study the shear behaviors of rocks (Heng et al., 2015; Saiang et al., 2005), was also employed to study the shear strengths and failure characteristics of shale. Several scholars (Heng et al., 2015; Lu et al., 2021b) conducted direct shear tests on Longmaxi shale with different bedding angles (i.e., $\theta = 0°$, 30°, 60° and 90°, where θ is the angle between the shear plane and the bedding plane) and investigated the influences of bedding planes on the shear failure behaviors. It was found that the shear parameters, including peak strength τ_p, cohesion c and internal friction angle φ, and the fracture surface morphology exhibit significant anisotropies. Furthermore, the failure patterns are divided into shear failure along the bedding planes (when $\theta = 0°$) and across the bedding planes (when θ is 30°, 60° and 90°). In addition, Yan et al. (2017) studied the chemical effects of drilling fluids on the shear strength of shale matrix and bedding planes through direct shear tests. Carey et al. (2015) and Frash et al. (2016) highlighted the anisotropic fracture-permeability behavior of Utica shale by preforming triaxial direct-shear experiments. The aforementioned works clearly reflected the presence of anisotropies in the shear failure behaviors. Nevertheless, the 3D anisotropy in shear failure of shale has never been reported.

As shown in Fig. 1a–d, the bedding angle was only varied in a 2D plane for both compression and direct shear tests in most existing studies. In engineering practice, shear failure in the instability of horizontal wells and hydraulic fracturing processes is generally multifarious and usually influenced by the local in situ stress field, dip of the shale formation and distribution of natural fractures. In addition, it was reported that the 3D spatial effect of foliation on the tensile failure behaviors of slate is significant (Ding et al., 2021). Therefore, the 3D anisotropy in the shear failure of shale should be highlighted. As shown in Fig. 1e, the bedding orientation should be defined in 3D space, with both in-plane angle θ (angle between the shear plane and bedding plane) and out-plane angle β (angle between bedding plane and right surface of the specimen). In the rock fracture mechanics field, three principal crack propagation orientations are defined to investigate 3D anisotropy: arrester, divider and short-transverse orientations (Chong et al., 1987). Referring to the definition of principal crack propagation orientations in fracture mechanics, as depicted in Fig. 1f–h, three typical bedding orientations in direct shear tests can be defined: (1) the arrester orientation, when the normal of the bedding plane is along the shear direction (i.e., $\theta = 90°$ and $\beta = 0°$); (2) the divider orientation, when both the bedding plane and normal of the bedding plane are perpendicular to the shear direction (i.e., $\theta = 90°$ and $\beta = 90°$); (3) the short-transverse orientation, when the normal of the bedding plane coincides with that of the shear plane (i.e., $\theta = 0°$ and $\beta = 0°$). As mentioned, most studies investigated the anisotropies in the shear strength and failure pattern of shale rocks when θ varies from 0° to 90° with $\beta = 0°$ (i.e., from the short-transverse orientation to the arrester orientation). However, experimental data on the shear failure of shale rocks with the divider orientation are rare, so determining these anisotropies in 3D space is important.

Aiming at the fact that the 3D anisotropy of the shear failure of shale remains unclear, the anisotropic shear failure characteristics of Longmaxi shale under different bedding angles and normal stress levels were systematically studied. Direct shear tests on shale samples with three typical bedding angles were performed, i.e., the arrester, divider and short-transverse orientations. The acoustic emission (AE) technique has been proven to be very effective in locating microcracks in rocks and the digital image correlation (DIC) technique can capture a high-resolution measurement of the surface displacement field of a deformed solid, so both techniques were employed to continuously acquire data of the damage evolution in real time during each test. To obtain insight into the

anisotropic shear failure of shale, the fractures inside the typical ruptured shale samples were observed and reconstructed using the X-ray CT technique. With a combination of AE, DIC, and CT techniques, the anisotropies in the shear mechanical properties and failure characteristics were comprehensively investigated from the outside to the inside of each sample, which offers some new results on the shear failure of shale.

2. Experimental

2.1. Material and samples

The tested Longmaxi shale was taken from a large outcrop block collected from Shizhu County, eastern Chongqing, China. The dry density of the studied shale was approximately 2.47 g/cm^3. The P-wave velocities perpendicular to the bedding planes and parallel to the bedding planes were 4196.25 m/s and 4591.89 m/s, respectively, which corresponded to an anisotropy ratio of 1.09. X-ray diffraction (XRD) analysis indicates that clay and quartz were the dominant minerals in the tested shale, with contents of 50 wt% and 42 wt%, respectively, and there was a small amount of aluminosilicate (5 wt%), followed by dolomite (2 wt%) and pyrite (1 wt%). A series of uniaxial compression tests with different bedding angles (angle α between axial loading direction and normal to the bedding plane) were conducted on cuboid shale specimens (50 mm $\times$ 50 mm $\times$ 100 mm). During each test, the axial force was collected by the force transducer and the strains were measured with the strain gauges. With the iterative method to approach the crack initiation stress threshold (He et al., 2022), the average characteristic stresses and uniaxial compression strength (UCS) of the tested shale were obtained (see Table 1).

Cubic shale samples with side lengths of 50 $\pm$ 0.1 mm were prepared. To prevent the influence of cooling water on the mechanical properties of the studied shale during manufacturing, the samples were cut and polished under dry conditions. During sample preparation, each two adjacent faces of a sample were made perpendicular to each other. To investigate the 3D anisotropy in the shear failure of shale, three typical bedding orientations were considered: the arrester, divider and short-transverse orientations, as shown in Fig. 1f–h. In addition, it is known that the applied normal stress plays an important role in the shear failure behavior of rock. Therefore, three normal stress levels were considered for each bedding angle: $\sigma_n = 10$, 30 and 50 MPa; for each normal stress condition, 4 samples were tested, which yielded 36 samples in total. Typical samples are shown in Fig. 2.

2.2. Procedures

2.2.1. Direct shear test

The shear tests on the Longmaxi shale were performed at the Key Laboratory of Deep Earth Science and Engineering, Sichuan University. A direct shear test system with normal and horizontal capacities of 500 kN and 1000 kN, respectively, was adopted. For each test, the applied normal force (i.e., F_n in Fig. 3) was loaded to a predetermined value with a loading rate of 20 kN/min, and during the shear loading stage, the normal loading remained immutable. In this work, since the applied normal stresses were 10, 30 and 50 MPa, the applied normal forces were calculated as 25, 75 and 125 kN using the equation of $F_n = \sigma_n \times A_s$, where A_s is the area of the shear plane of a sample in Fig. 3. After the initial normal load was applied, the shear force (i.e., F_s in Fig. 3) was loaded under a displacement control mode at a rate of 0.1 mm/min. The shear loading continued until the sample was completely ruptured and the shear force no longer decreased. All samples were tested at room temperature.

2.2.2. AE monitoring

AE monitoring is an effective method to inspect the generation of microcracks inside a rock specimen under stress. The characteristic stress thresholds, e.g., the crack initiation stress and crack damage stress, can be accurately identified by interpreting the evolution of the AE parameters (Moradian et al., 2010; Zhang et al., 2020a; Zhao et al., 2015). In this work, a PCI-II AE system produced by Physical Acoustics Corporation was employed to monitor the damage evolution of Longmaxi shale during each shear test. Eight AE sensors were fixed on the upper and lower end faces of the sample, as depicted in Fig. 3. The AE sensors have a working frequency band of approximately 1 kHz–3 MHz. Based on a preliminary analysis of the collected signals, a detection threshold of 40 dB was adopted. Notably, the friction between an AE sensor and the sample surface might cause an error of measurement, and petroleum jelly was employed to daub and cover the AE sensors to guarantee good coupling and eliminate the friction between AE sensor and sample surface.

2.2.3. DIC monitoring

The DIC method is a noncontact measurement technique that provides a full-field displacement of a target surface of a deformed solid by correlating the digital images acquired during loading (Lin et al., 2020; Miao et al., 2021; Zhu et al., 2019). In this work, the VIC-3D test system, which contains two high-precision cameras with 1024 $\times$ 1280 pixels, two light sources and a controller, was used to obtain displacement field data and calculate strain field. Before each test, the front free surface of the sample was coated with a white paint layer of uniform thickness and subsequently sprayed with black paint to generate a random speckle pattern. The target surface was ensured to have a nonrepetitive, isotropic, high-contrast pattern. During the test, each camera captured 1 image per 4 s at the initial loading stage and subsequently 5 images per second when the sample was approaching destruction. After the test, the surface displacement and strain fields were calculated with the postprocessing software VIC-3D, and the calculation accuracies of displacement and strain were 0.01 pixels and 50 $\mu\varepsilon$, respectively.

2.2.4. X-ray CT scanning

The CT scanning technique was introduced into the field of rock mechanics to visualize the fractures, pores and minerals inside rock samples, which provided a possible method to “see” the failure mechanism of rocks (Shen et al., 2021; Zhang et al., 2018, 2020b). After the shear tests, some typical ruptured samples were scanned using the industrial CT scanning system V|Tome|X L 300 at Sichuan

Table 1
Average characteristic stresses and uniaxial compression strength of the tested shale.

Bedding angle α, °	Crack initiation stress σ_{ci}, MPa	Crack damage stress σ_{cd}, MPa	UCS, MPa
0	26.38	82.22	117.89
45	24.20	67.77	79.42
90	31.04	106.73	128.30

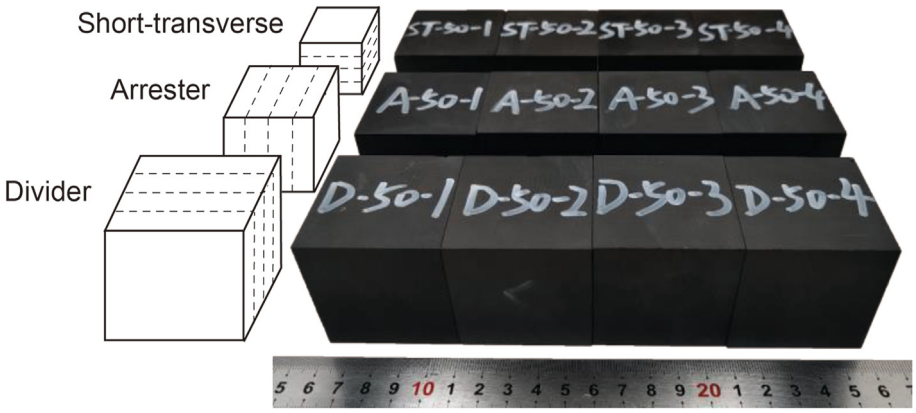

Fig. 2. Typical shale samples.

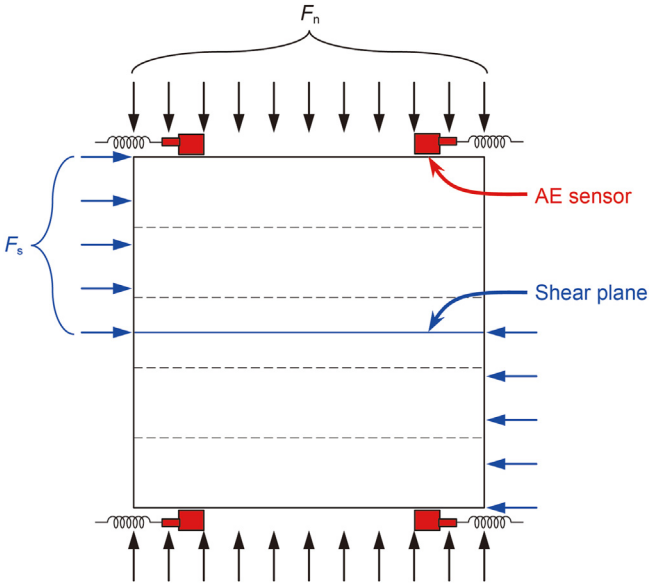

Fig. 3. Sketch of the shear loading condition of shale and arrangement of AE sensors.

University, which collects images along the normal central axis using a multislice helical CT scan method. To obtain high-quality images, the helical CT scan method was implemented over an equal increment angle per step using a slow sample rotation speed, and it produced approximately 1700 CT scan images per sample. Considering the sample size and scanning rotation speed, the scanning resolution in this work was approximately 42 μm with a single exposure time of 500 ms, so the X-ray source power was set to 240 μA and 220 kV. Finally, the 3D fractures inside a cubic shale sample were obtained after the reconstruction and processing of 1700 CT images for detailed analysis.

3. Results and discussion

3.1. Anisotropy in the shear strength

3.1.1. 3D anisotropy in the peak strength

During shear loading, the shear stress τ_s acting on the shear plane in a shale sample was calculated as $\tau_s = F_s/A_s$. Typical shear stress–shear displacement curves are shown in Fig. 4. Once the peak shear strength (τ_p) was reached, the shear stress dropped to a certain value, i.e., the residual shear strength (τ_r), and subsequently remained unchanged or slightly increased. Some small fractures resulted in the formation of block fragments and spalling and consequently reduced the net area of the macroscale shear plane, i.e., the obtained residual strength is actually a nominal residual strength (τ_{rn}). The peak shear strengths and nominal residual strengths of samples under different bedding orientations and normal stresses are shown in Table 2, where the nominal residual strengths of samples #ST-50-1 and #ST-50-3 are absent because they were not loaded to the post-peak stable stage. The heterogeneity of the shale rock results in the differences in each sample, which leads to the dispersion of the experimental results (Huang et al., 2020). Dixon's test (Dixon, 1950) was used to eliminate the outliers of peak strength, and the significance level α was set to 5%. Accordingly, the peak shear strengths of samples #A-10-4 and #ST-30-3 were detected as outliners and removed for further analyses.

The peak shear strength results are plotted in Fig. 5, and a significant 3D anisotropy was observed. Under identical normal stress levels, the divider samples have greater average peak shear strength than the arrester samples, and the short-transverse samples have the minimum average peak shear strength. The shear strength of the arrester sample is 15.37%, 6.93% and 4.04% larger than those of the short-transverse sample for normal stresses of 10, 30 and 50 MPa, respectively. In contrast, the shear strength of the divider sample is 6.22%, 15.96% and 8.22% larger than those of the short-transverse sample with the normal stresses of 10, 30 and 50 MPa, respectively. Clearly, the out-of-plane angle β significantly affects the peak shear strength, especially when the normal stresses are 30 MPa and 50 MPa. This result demonstrates that it is insufficient to reveal the anisotropic shear failure of shale rocks in 2D space, and it is critically important to discuss the anisotropy in the shear strength in 3D space.

The shear strength parameters, i.e., cohesion c and internal friction angle φ in the Mohr-Coulomb (MC) criterion, were determined by linear regression between the peak strengths τ_p and the applied normal stresses σ_n (see Fig. 5). The divider sample has the largest observed cohesion, which is 32.79 MPa, followed by the arrester sample with 29.83 MPa. In comparison, the short-transverse sample exhibits a minimum value of 23.85 MPa, which is significantly smaller than that of the samples with the other two bending orientations. Unexpectedly, the short-transverse samples do not have the smallest observed internal friction angle. The internal friction angles of the arrester, divider and short-transverse samples are 44.89°, 47.78° and 46.50°, respectively, which are quite similar.

In wellbore stability analysis and hydraulic fracturing technology optimization, the shear strength parameters are essential,

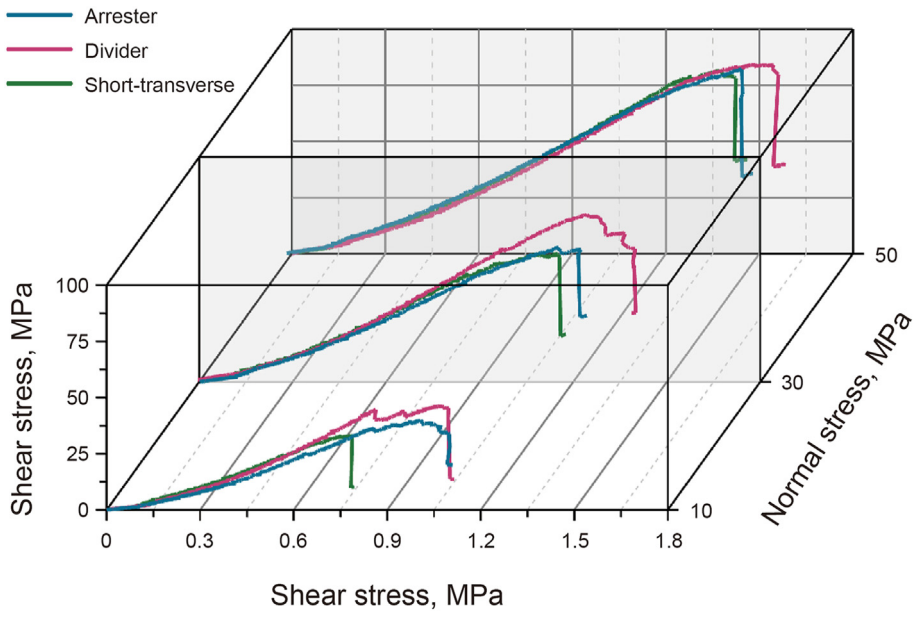

Fig. 4. Typical stress–displacement curves for different conditions.

Table 2
Direct shear strengths for different bedding orientations and normal stress conditions.

Sample no.	Bedding orientation	σ_n, MPa	τ_p, MPa		τ_{rn}, MPa	
			Individual	Average	Individual	Average
A-10-1	Arrester	10	38.84	39.07	18.37	23.43
A-10-2			39.83		19.91	
A-10-3			38.53		32.02	
A-10-4			46.89		24.77	
A-30-1		30	60.22	60.78	32.18	29.59
A-30-2			62.57		32.61	
A-30-3			60.49		24.68	
A-30-4			59.86		28.90	
A-50-1		50	78.74	79.09	37.90	33.75
A-50-2			75.68		32.09	
A-50-3			82.10		33.99	
A-50-4			79.84		31.03	
D-10-1	Divider	10	44.36	41.50	23.71	18.83
D-10-2			35.29		22.74	
D-10-3			46.21		13.61	
D-10-4			40.13		15.24	
D-30-1		30	65.34	70.49	26.70	29.30
D-30-2			74.30		30.67	
D-30-3			74.99		25.26	
D-30-4			67.32		34.57	
D-50-1		50	85.49	85.59	44.11	39.98
D-50-2			86.95		37.75	
D-50-3			84.13		38.77	
D-50-4			85.78		39.28	
ST-10-1	Short-transverse	10	32.88	33.87	9.81	14.62
ST-10-2			36.46		25.41	
ST-10-3			33.30		11.17	
ST-10-4			32.82		12.09	
ST-30-1		30	57.05	56.84	20.31	23.79
ST-30-2			56.47		25.17	
ST-30-3			47.93		31.89	
ST-30-4			57.01		25.89	
ST-50-1		50	73.12	76.01	–	39.31
ST-50-2			72.84		37.51	
ST-50-3			76.57		–	
ST-50-4			81.53		41.10	

whether theoretically or numerically (Chen et al., 2021a; Ma et al., 2020). In wellbore stability analysis, the isotropic approach using the Kirsch solution is widely used because it is convenient for the practical implementation (Kirsch, 1898). However, it was demonstrated that suboptimal predictions of borehole failure might be caused by neglecting the anisotropic strength parameters of shale

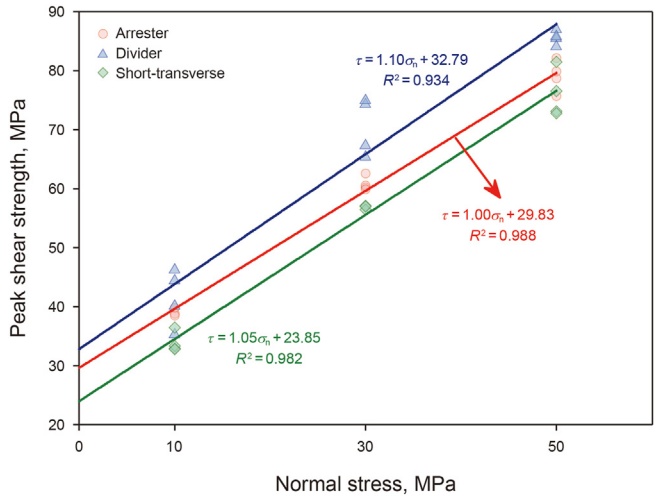

Fig. 5. M-C envelopes of shale for three typical bedding orientations.

(Asaka and Holt, 2020). Therefore, the 3D anisotropies in shear strength parameters should be seriously considered in engineering practice. Due to the complexity of predicting the induced fracture network, it is critical to conduct hydraulic fracturing simulations (Chen et al., 2021a). When simulating fracture propagation with smeared fracture models, the MC failure criterion is normally adopted to determine the initiation and propagation of shear fracture (Li et al., 2012). For discontinued-based methods, the fracture is represented by the breakage of bonds between particles or blocks. The results of this section also provide vital information to calibrate the microparameters.

3.1.2. 3D anisotropy in the residual strength

The nominal residual strengths of shale with different bedding orientations and normal stress conditions are shown in Fig. 6. The observed anisotropy in nominal residual strength is different under different normal stress conditions. When the normal stress σ_n is 10 MPa, the nominal residual strength of arrester sample $\tau_{rn,A}$ is the maximum, followed by those of divider sample $\tau_{rn,D}$ and the short-transverse sample $\tau_{rn,ST}$, i.e., $\tau_{rn,A} > \tau_{rn,D} > \tau_{rn,ST}$. When $\sigma_n = 30$ MPa, the arrester and divider samples have very similar nominal residual

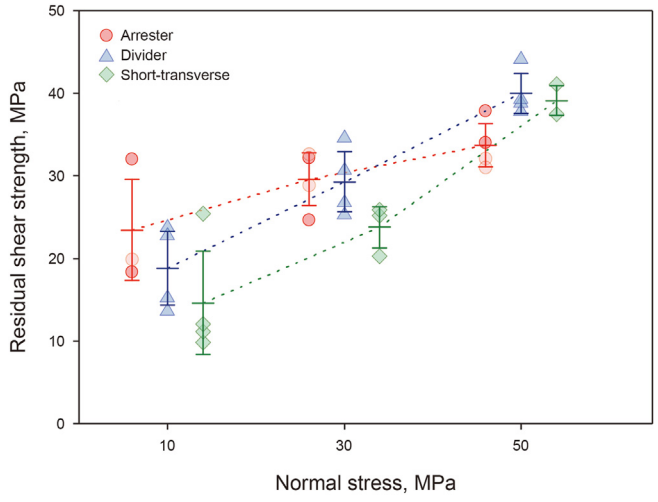

Fig. 6. Nominal residual strengths with different bedding orientations and normal stress conditions.

strengths. Interestingly, the ranking of nominal residual strengths becomes $\tau_{rn,D} > \tau_{rn,ST} > \tau_{rn,A}$, which is quite different from that under low normal stress conditions.

According to Amontons' friction law, the residual strength of a given rock significantly depends on the friction coefficients of the fracture surfaces (Jaeger et al., 2009). The friction coefficient of a fracture is directly proportional to the roughness of the fracture surfaces; thus, the residual strength anisotropy can be further interpreted by comparing the fracture surface morphologies of the ruptured samples with three typical bedding orientations. As shown in Fig. 7a, a macrofracture surface with many small inclined en echelon fragments, which exhibited a "factory roof" profile, was observed for the arrester sample, and this phenomenon became more significant with the increase in the applied normal stress, which resulted in a rougher shear failure surface. For the divider sample, the fracture surface undulated in the shear direction and appeared much flatter than that of the arrester sample for each normal stress condition tested. As shown in Fig. 7, a higher normal stress usually results in a more fluctuating fracture surface. In addition, a macroscale tensile crack parallel to the bedding was observed penetrating into the divider sample under the normal stress of 50 MPa. For the short-transverse samples, the fracture surfaces are relatively flat but not smooth, as indicated in Fig. 7c. In general, for the arrester and divider orientations, a larger applied normal stress corresponded to a rougher fracture surface, while for the short-transverse orientation, a visual inspection suggests that the shear fracture surface morphology almost does not change with the normal stress. From the results in Fig. 7, it is easy to conclude that under a specific normal stress condition, the arrester (short-transverse) sample has the roughest (flattest) fracture surface. If Amontons' friction law holds true, the arrester (short-transverse) sample should have a maximum (minimum) residual strength for all normal stress conditions, which is inconsistent with the fact that the divider (arrester) sample exhibits a maximum (minimum) nominal residual strength for $\sigma_n = 50$ MPa. Therefore, this issue requires further discussion.

As depicted in Fig. 7, the integrity of a ruptured sample worsens with increasing normal stress. For example, the two pieces of the ruptured sample are almost complete for each bedding orientation at $\sigma_n = 10$ MPa, while some small fractured blocks spall from each sample during shearing when $\sigma_n = 50$ MPa. The spalling of the fractured blocks will reduce the area of the shear fracture surface. In other words, the net shear fracture surface area that can provide shear resistance decreases due to the spalling of the fractured blocks, which decreases the nominal residual strength. The arrester and divider ruptured samples have much worse integrity than the short-transverse sample for a specific normal stress. This result explains the lower nominal residual strength for the sample with a rougher fracture surface. Therefore, the nominal residual strength calculated by the initial shear area cannot truly reflect the residual shear resistance of shale rocks. Considering the influence of sample integrity nominal residual strength, the ranking of the true residual strengths for the three typical bedding orientations under a high normal stress should be consistent with that under a low normal stress, i.e., $\tau_{r,A} > \tau_{r,D} > \tau_{r,ST}$.

3.1.3. Remarks on shear strength of the Longmaxi shale

To date, several studies have measured the shear parameters of Longmaxi shale using direct shear tests, and the results are summarized in Table 3. Unfortunately, to the best of our knowledge, the shear strength parameters of the divider sample have not been measured for the Longmaxi shale formation, and the related datasets were, therefore, absent. The results show that the shear strength parameters and corresponding anisotropy ratios are quite different. Generally, the shear strength parameters for the arrester

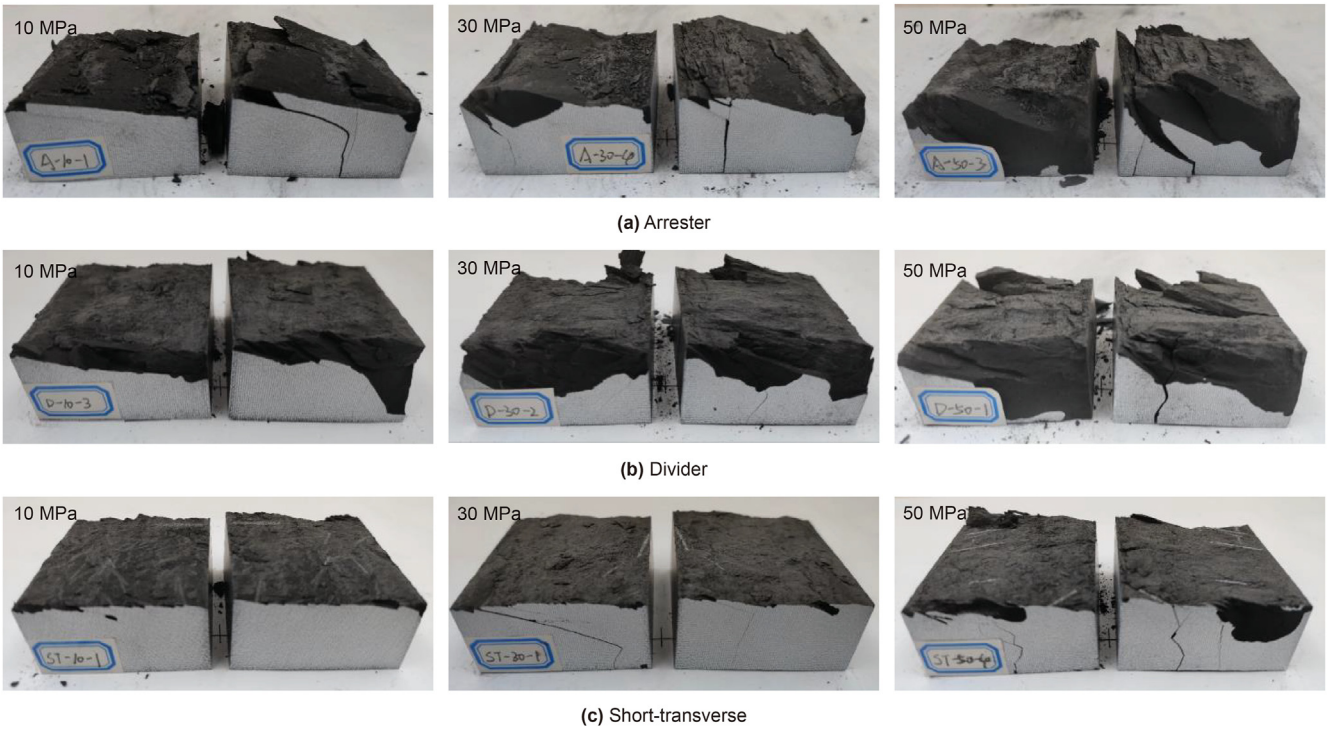

Fig. 7. Fracture surface morphologies of typical ruptured shale samples.

Table 3
Summary of the shear strength parameters of Longmaxi shale.

Resource	Bedding orientation	c, MPa	φ, °	c_A/c_{ST}	c_A/c_D
This work	Arrester	29.83	44.89	1.25	0.91
	Divider	32.79	47.78		
	Short-transverse	23.85	46.50		
Lu et al. (2021b)	Arrester	31.15	27.11	1.60	–
	Short-transverse	19.49	32.94		
Heng et al. (2015)	Arrester	16.04	35.34	1.80	–
	Short-transverse	8.92	32.31		
Yan et al. (2017)	Arrester	25.22	32.24	5.14	–
	Short-transverse	4.91	25.90		

orientation are considered those of the shale matrix (Heng et al., 2020). However, the peak shear strength, cohesion and internal friction angle were found to reach their maximums at the divider orientation for the tested shale. Clearly, the bedding orientation that enables one to obtain the shear strength parameters of the shale matrix should be further discussed. Concerning the cohesion, as shown in Table 3, the anisotropy ratio of the cohesion of the arrester sample to that of the short-transverse sample, which is denoted by c_A/c_{ST}, is 1.25 in this study. However, ratios of 1.60, 1.80 and 5.14 were obtained by Lu et al. (2021b), Heng et al. (2015), and Yan et al. (2017), respectively. In this study, the cohesion anisotropy ratio for the arrester and divider orientations, c_A/c_D, was 0.91. In addition, the internal friction angle of Longmaxi shale reaches its minimum at the short-transverse orientation in both Heng et al. (2015) and Yan et al. (2017), whereas the internal friction angle of the short-transverse sample is larger than that of the arrester sample in this work and Lu et al. (2021b). There are several possible explanations for these differences. First, although the shales tested in different studies were collected from Longmaxi shale formation outcrops, different contents of the dominant minerals (clay and quartz) were found. For example, the clay content was 50 wt% in this work, while contents of 34.2 wt% in Lu et al. (2021b) and 41.9 wt% in Yan et al. (2017) have also been determined. Such differences in mineral contents may lead to different experimental results. Second, as depicted in Fig. 8, the sample configuration and experimental boundary conditions are different. In this work and Lu et al. (2021b), a cubic sample configuration was adopted, while a cylindrical configuration was employed by Heng et al. (2015) and Yan et al. (2017). In particular, the horizontal loading (in Fig. 8b), which can generate the shear force in the middle cross-section of the shale sample, may not have been uniformly applied on the sample surface in the work of Heng et al. (2015); similarly, the normal loading (in Fig. 8c), which was employed to apply the normal stress on the shear plane, may not have been uniformly applied on the sample surface in the work of Yan et al. (2017). Finally, although the short-transverse sample was more likely sheared along the bedding than other samples, strict sliding failure along the bedding was not observed in this work. A similar conclusion was drawn by several studies. Niandou et al. (1997) found that when θ was 30–75°, failure by sliding along bedding occurred under only low confining pressure conditions in triaxial experiments. Keneti and Wong (2011) found that when the orientation of shear was parallel to the bedding, the sample did not necessarily shear along the bedding planes and instead behaved like an intact rock, especially under high normal stresses. In other words, the weak bedding planes are tightly compacted under a high normal stress, and the short-transverse sample does not have exactly equal peak shear strength to the bedding plane.

3.2. Anisotropy in the progressive shear failure process

3.2.1. Characterization of the shear failure process combined with AE and DIC monitoring

Progressive fracturing occurs during rock failure (Lei et al., 2020; Zhang et al., 2019), which leads to an evolution of damage during loading. Shear dilation is associated with microcrack initiation and propagation when the rock is loaded beyond a certain threshold

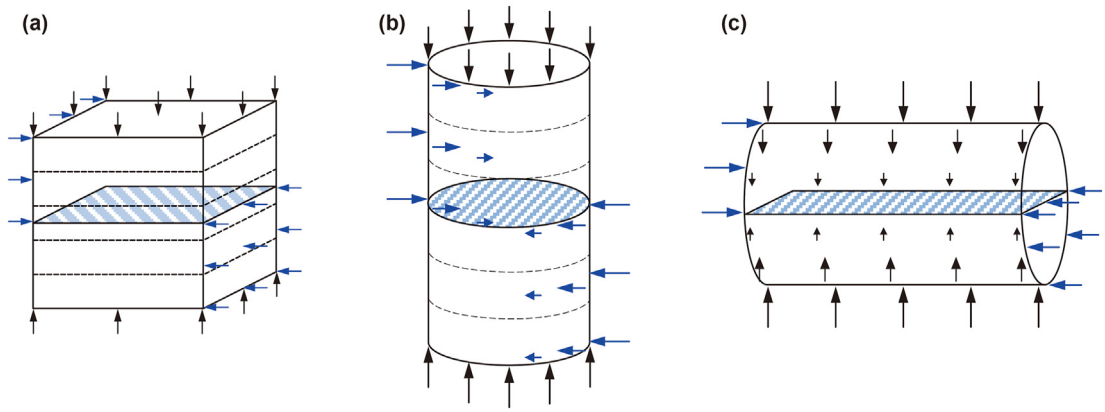

Fig. 8. The sample configurations and experimental boundary conditions of direct shear tests: (a) this work and Lu et al. (2021b); (b) Heng et al. (2015); and (c) Yan et al. (2017).

(Zhao and Cai, 2010). For the direct shear test, the normal displacement changes to maintain the normal load during shearing, and the upward normal displacement is defined as the dilatancy displacement (Zheng et al., 2021). To comprehensively investigate the fracture characteristics and reveal the mechanism of shear failure, the evolutions of the applied shear stress, dilatancy displacement, AE activity and surface strain field during shearing were analyzed together, and the analysis and discussion of the results of sample #ST-30-1 are provided below as an example, as shown in Fig. 9. Through a combined analysis of the shear stress, normal dilation displacement, AE activity and surface strain field, the progressive shear failure process was divided into five stages: the initial stage (OA), elastic deformation stage (AB), crack stable propagation stage (BC), crack coalescence stage (CD) and postpeak stage (DE).

At the initial stage, the microcracks inside the shale sample were rearranged by shearing under the initial shear stress (the microcracks were previously compacted by the vertical applied normal stress). Notably, there was almost no shear dilation during the initial stage. When the loading continued to the elastic deformation initiation stress level, an obvious turning point A appeared in the shear stress curve, which indicated the end of the initial shear stage and the beginning of the elastic deformation stage. At the elastic deformation stage, both shear stress and dilatancy displacement curves almost linearly increased, which reflects that the sample was undergoing elastic deformation. At the initial and elastic deformation stages, the surface strain field was not uniform due to the heterogeneity of shale rock, and no obvious high strain localization was observed. In addition, few AE events were detected, and the corresponding AE count rate and energy rates were quite low.

The time at which shear dilation starts does not always coincident with the beginning of elastic deformation. To further investigate the effect of the applied normal stresses on the shear dilation, the shear dilation-displacement curves of the short-transverse samples under three normal stress conditions were fitted by polynomials, as shown in Fig. 10. Clearly, the increase in applied normal stress reduced the peak shear dilation and affected the timing of shear dilation. Dilation started from the beginning of loading under the normal stress of 10 MPa, while under the normal stress of 30 MPa, the occurrence of shear dilation was significantly delayed. When the normal stress was 50 MPa, the shale sample underwent slight shear compression followed by shear dilation.

When the applied shear stress reached point B, the internal microcracking inside the sample became active, and the sample no longer exhibited linear elasticity. Thus, the shear stress at point B could be named the crack initiation stress threshold. Due to limited space, in Fig. 9, only the cumulative AE energy curve of stage BC was enlarged. Before point B, the number of cumulative AE counts was only 97, and the cumulative AE energy was 0.2 aJ. At point C, the number of cumulative AE counts increased to 473, and the cumulative AE energy increased to 4.5 aJ (almost 22 times that before point B). This result indicates that both the number and intensity of AE activity significantly increased at stage BC. Since the shear stress continued to increase steadily, stage BC was defined as the crack stable propagation stage, during which, an elliptical shear band gradually formed in the middle of the sample. In addition, the dilatancy displacement curve deviated from the trend line of the dilation curve at the elastic deformation stage, which indicates that the sample began to inelastically deform.

When the applied shear stress reached point C, the microcracking in the shear band started to coalesce, an inclined macrocrack was generated in the middle of the sample, and the shear stress at point C could be defined as the crack coalescence stress threshold. The shear band appeared to be formed by extension since the surface strains in the shear band were positive according to the surface strain field at point C measured by the DIC method. However, the generated macrocrack intersected the potential shear plane at a small angle. Under the constraint of normal stress, the macrocrack could not be induced by tensile stress but could be induced by shear stress. The positive strain in the shear band may be caused by the shear slip on the inclined shear microcracks. When loading continued, the crack was compacted and no longer propagated due to the friction induced by the normal stress. The stress field inside the sample was redistributed; then, high-strain bands formed at the two ends of the shear zone due to the stress concentration induced by the contacts between the sample surfaces and the shear box. Accordingly, new inclined edge cracks initiated and propagated from the two ends of the shear zone to the middle of the sample. During this stage, the cumulative AE counts and energy dramatically increased, mainly due to the initiation and propagation of wing cracks and the frictional sliding of the formerly generated crack surfaces. The cumulative AE count curve and cumulative AE energy curve at this stage showed different characteristics. The cumulative AE count increased with a relatively stable slope, while the cumulative AE energy exhibited several significant step-like jumps (normally, each large jump in AE energy corresponded to large-scale crack propagation). For each AE energy jump, the shear stress dropped and continued to rise, which was essentially induced by edge crack propagation. Meanwhile, the slope of the dilatancy displacement curve further increased, which indicates that the dilation effect was accelerated.

Point D corresponded to the peak shear stress; before this point,

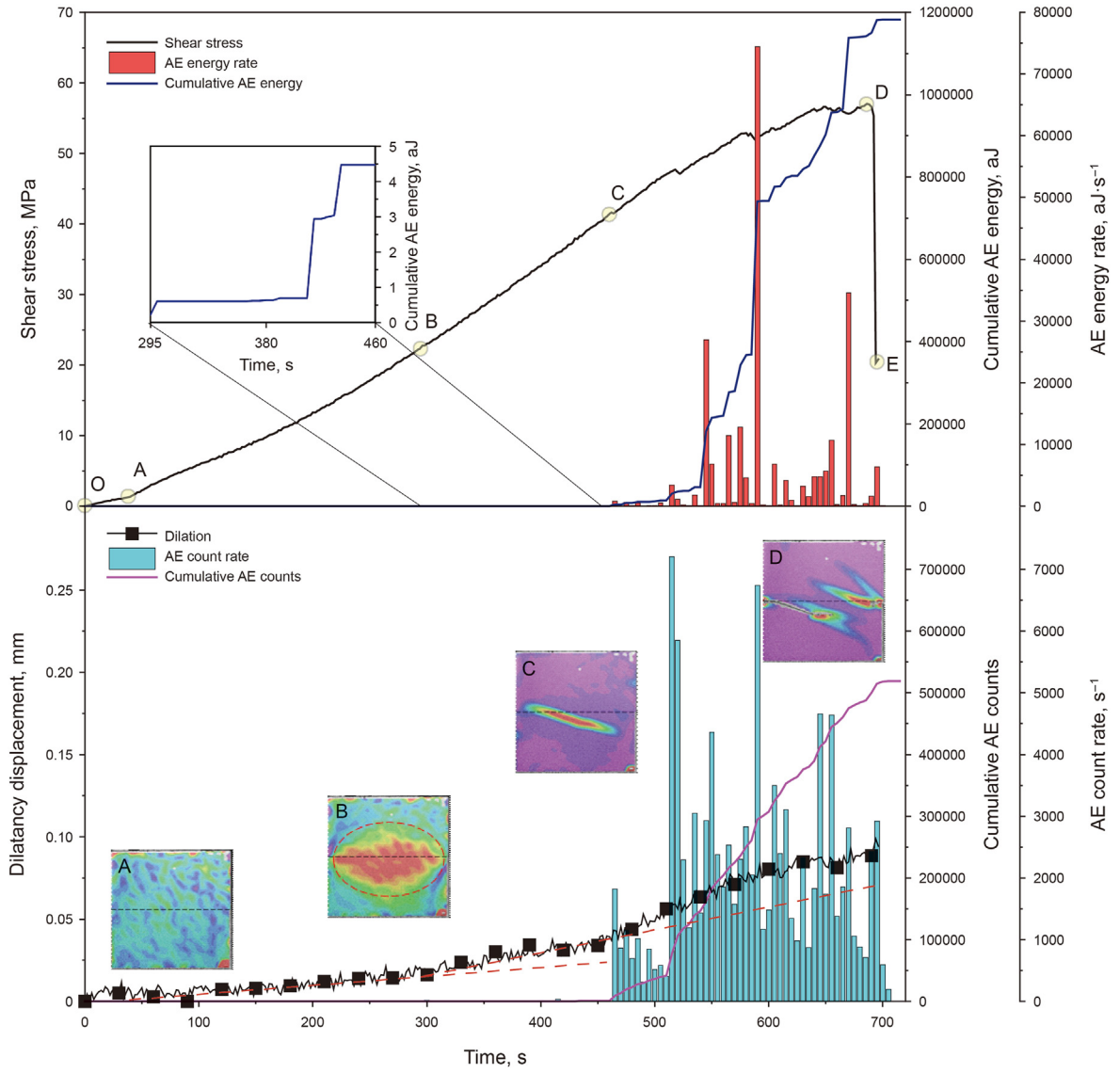

Fig. 9. Evolution of the shear stress, dilatancy displacement, AE activity and major principal strain in sample ST-30-1.

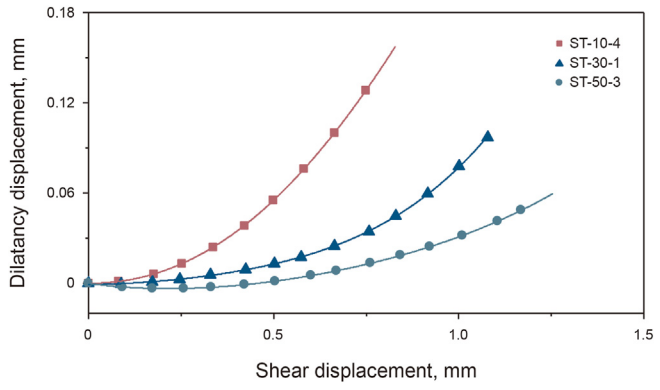

Fig. 10. Dilatancy displacement curves recorded under different normal stresses.

the shear plane was seriously damaged, as shown by the major principal strain contours. When the loading reached the peak stress, the sample instantaneously underwent macroscopic shear failure, and the shear stress rapidly dropped to the nominal residual stress, which indicates a typical brittle failure manner.

The above analyses show a close relationship among the shear stress, dilatancy displacement, AE activity and surface strain field, which enables one to define the shear stress threshold of each stage. Overall, shear failure in shale is a complex cracking process, and it is almost impossible to gain deep insight into such a progressive damage accumulation process with a single experimental method. In addition, the crack initiation and crack coalescence stress levels of each sample are shown in Fig. 11. The crack initiation and crack coalescence stress exhibited a larger dispersion than peak shear strength. Referring to the relationship between peak shear strength and normal stress, a linear trend line for each bedding orientation is plotted in Fig. 11. The crack initiation stress level was approximately 25%–45% and the crack coalescence stress level was approximately 50%–80%. Interestingly, characteristic stress levels showed anisotropy different from the peak shear stress. The arrester samples have the largest characteristic stress levels, and the divider samples have the smallest ones. The characteristic stress levels are insensitive to changes in applied normal stress.

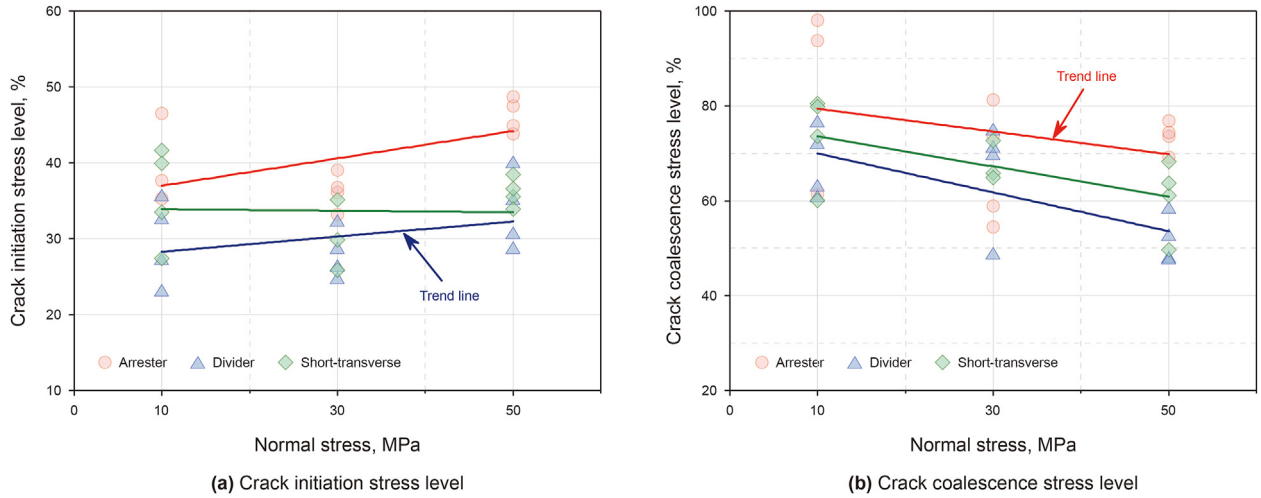

Fig. 11. Characteristic stress levels for different conditions.

When the normal stress increased, the crack initiation stress level slightly increased, while the crack coalescence stress level slightly decreased.

3.2.2. 3D anisotropy in the shear failure process

To investigate the effect of bedding on crack propagation, the crack evolution of typical samples at each loading point is shown in Fig. 12 (the letter at the top left-hand corner indicates the previously described shear stress threshold of each stage). For the short-transverse sample with $\sigma_n = 10$ MPa, an elliptical shear band was observed when the applied shear stress reached the crack initiation stress threshold, and with the increase in applied shear stress, a macrocrack in the sample middle was generated along the bedding when the crack coalescence stress was reached. In addition, an edge crack on the left side of the sample formed and continuously propagated during the loading process to the peak shear stress. Finally, nearly along the bedding, a macroscopic shear fracture appeared once the peak shear stress was reached. For the short-transverse sample with $\sigma_n = 50$ MPa, the elliptical shear band and macrocracks in the middle of the sample were not observed during loading. During the crack coalescence stage, two obvious stress concentration bands formed at the two sides of each sample, resulting in the formation of two edge cracks. When the applied shear stress reached its peak, the material between the two edge cracks was completely sheared, and macroscopic shear fracturing still occurred along the bedding. Although the arrester sample and divider sample had similar fracture behaviors to the short-transverse sample, a certain bedding effect on fracture propagation was observed. For instance, the cracks in the arrester samples were more likely to propagate along the bedding (Fig. 12d and e) and macroscopic shear fracture of the arrester sample between the two edge cracks occurred along a plane that deviated from the expected shear failure plane. Additionally, as indicated in Fig. 12d and e, a higher applied normal stress corresponds to a more significant deviation of the shear failure plane. For the divider sample under the normal stress of 50 MPa, a tortuous macrocrack was first generated in the middle of the sample; then, two edge cracks formed, and the sample was ultimately destroyed by the propagation of these three cracks. Clearly, the shear failure process of these shale rocks was significantly influenced by the bedding orientation and applied normal stress condition.

According to the results in Section 3.2.1, many AE events occurred once the shear stress reached the crack coalesce stress threshold, indicating that many microcracks were generated inside the sample. Hence, to investigate the anisotropic failure mechanism of shale under direct shear loading, the crack classification method based on AF and RA values was employed (Ohno and Ohtsu, 2010). The parameter AF (kHz) is the ratio of AE counts to duration, and RA (ms/V) is the ratio of AE signal rise time to amplitude. Generally, tensile cracks correspond to AE signals with larger AF values and smaller RA values, whereas shear cracks correspond to AE signals with smaller AF values and larger RA values, which are distinguished by the transition line AF = k·RA (see Fig. 13). The density maps of RA-AF data of typical samples are shown in Fig. 14, where the blue area has higher data density and the gray area has lower data density. The high density zone of RA-AF data for shale under direct shear loading exhibited anisotropy. When $\sigma_n = 10$ MPa, the RA values mainly concentrated in 0–1.2 ms/V for the arrester orientation, 0–0.8 ms/V for the divider orientation and 0–1.0 ms/V for the short-transverse orientation. The AF values were mainly in the range of 75–150 kHz. The exhibited anisotropy indicates different mechanisms for different bedding orientations. Furthermore, five different transition lines were chosen to investigate the AE mechanisms: k = 100, 200, 300, 400 and 500. The results in Table 4 indicated that (1) under identical applied normal stress conditions, the percentage of shear cracks for the short-transverse samples is the largest and that for the divider samples is the smallest; (2) for identical bedding orientations, the percentage of shear cracks increased when the normal stress increased.

The structure of bedding planes is the inherent reason for the anisotropic behaviors of shale. Due to the weak cementation, the beddings have lower tensile strength and shear strength than the shale matrix (Heng et al., 2020). For the short-transverse orientation, the potential shear plane is consistent with the bedding plane, so shear-mode microcracks along the shear plane are easier to generate. Fan et al. (2022b) found that tensile cracks along vertical beddings were generated under compression-shear loading. In the shear band of the arrester samples, shear-mode microcracks in the matrix and tensile-mode microcracks along the beddings were generated. They coalesce by inclined shear cracks resulting in en echelon fractures (see Fig. 7a). For the divider orientation, tensile microcracks are easier to generate since the free surfaces (the front and back surfaces) are without constraints. Therefore, the short-transverse samples have the largest percentage of shear cracks, and the divider samples have the smallest one. The tensile-mode microcracks may consist of two parts. Some of them are

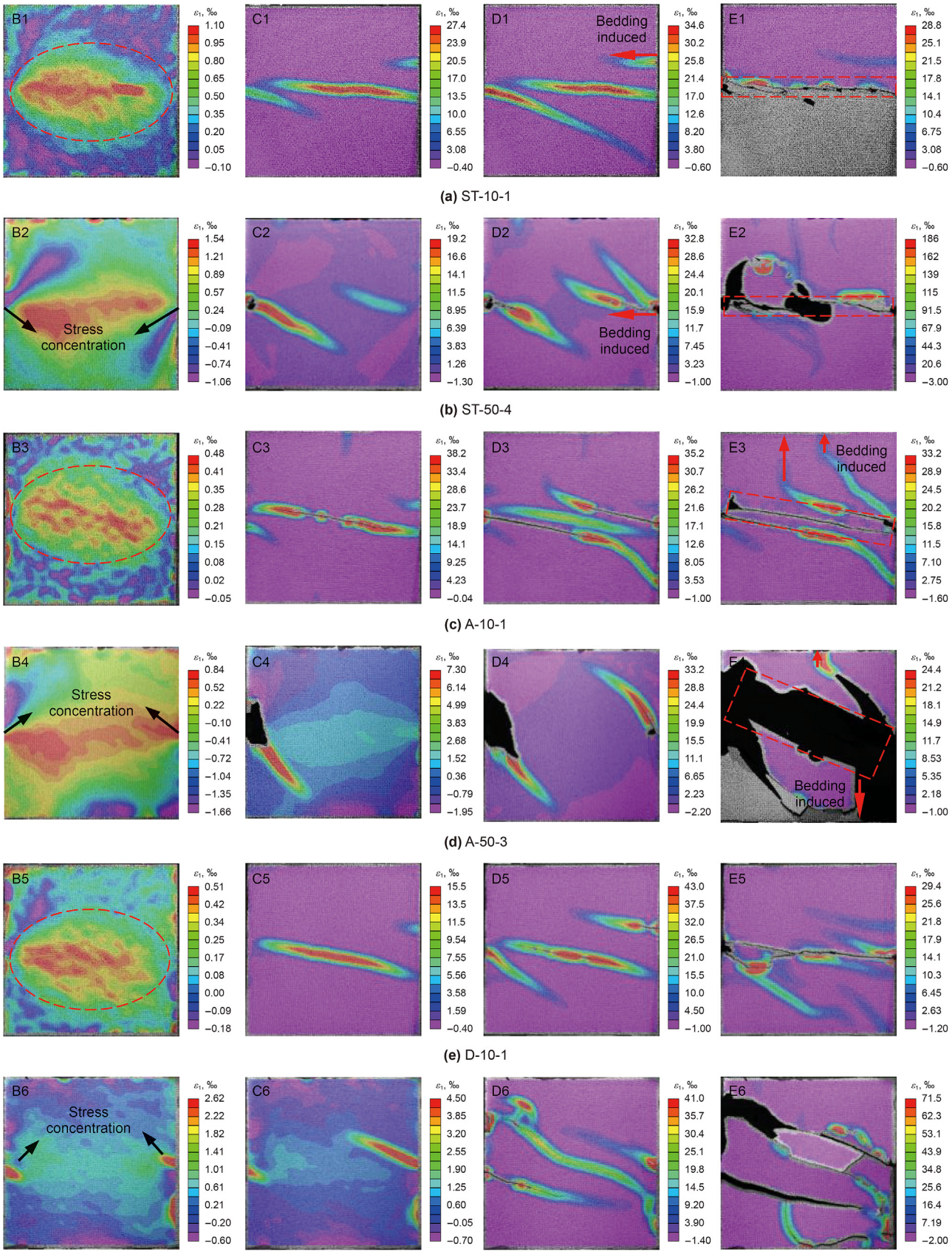

Fig. 12. Maximum principal strain contours of typical samples during shearing.

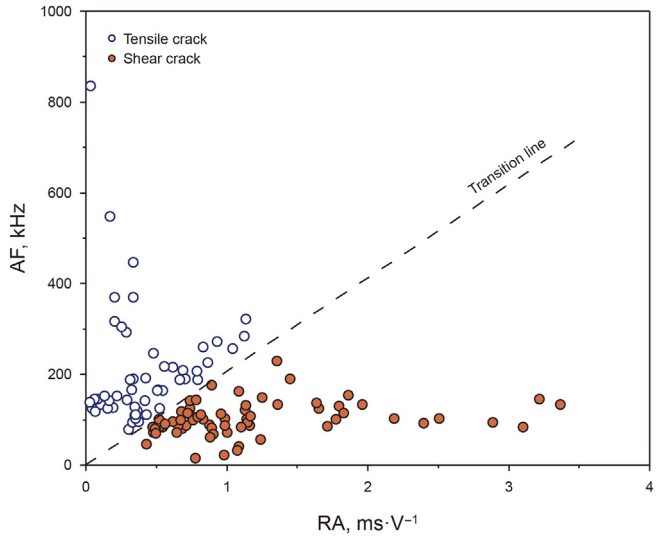

Fig. 13. Crack classification based on the ratio of AF to RA (after Aggelis, 2011).

generated during the propagation of the edge cracks. In addition, the coplanar shear cracks may also be coalesced by tensile cracks, i.e., the shear-tension-shear coalescence mode, due to the effect of shear dilation (Zhang et al., 2021b). When the normal stress increases, the shear-tension-shear coalescence is restrained, resulting in a higher percentage of shear cracks. Damage to the beddings is the essential reason for the anisotropic shear strength of shale. For the short-transverse sample, shear failure along the bedding plane minimizes its strength. For the arrester sample, tensile bedding-based microcracks make its shear strength smaller than that of the shale matrix. For the divider sample, tensile bedding-based microcracks only make the spalling behavior near the free surfaces more severe. When simplified to an in-plane problem, the shear failure of the shale matrix will consume the maximum energy. Therefore, the minimum shear strength was observed with the short-transverse orientation, and the maximum shear strength was obtained with the divider orientation, which should be considered as the shear strength of the shale matrix.

The optimal transition line differs for different materials, loading conditions and AE equipment settings. For example, the coefficient k is 200 for concrete (Ohno and Ohtsu, 2010), 100 to 150 for marble under uniaxial tension (Zhu et al., 2022) and 100 to 500 for brittle rocks under compression (Zhang and Deng, 2020). Hence, the determination of the optimal transition line is essential. The methods to determine the transition line can be divided into two categories. One category is to first determine the percentages of tensile- and shear-mode events using other methods; then, the optimal coefficient k is determined by approaching the percentages. For example, Ohno and Ohtsu (2010) determined the optimal k of concrete based on simplified Green's functions for moment tensor analysis; Zhang and Deng (2020) obtained the optimal k of different brittle rocks based on dominant frequency analysis. The other category is to determine the transition line according to known or hypothetical mechanisms. For example, Du et al. (2020) determined the transition line to make the AE events in the tension test mainly tensile-mode while those in the shear test are mainly shear-mode. Chen et al. (2021b) indicated that AE signals with smaller AF and smaller RA values represent mixed tension-shear cracks, so AE events could be divided into shear-, tensile- and mixed-modes using two parameters: the thresholds of AF and RA. The thresholds were determined according to the known mechanism that shear-mode microcracking became dominant

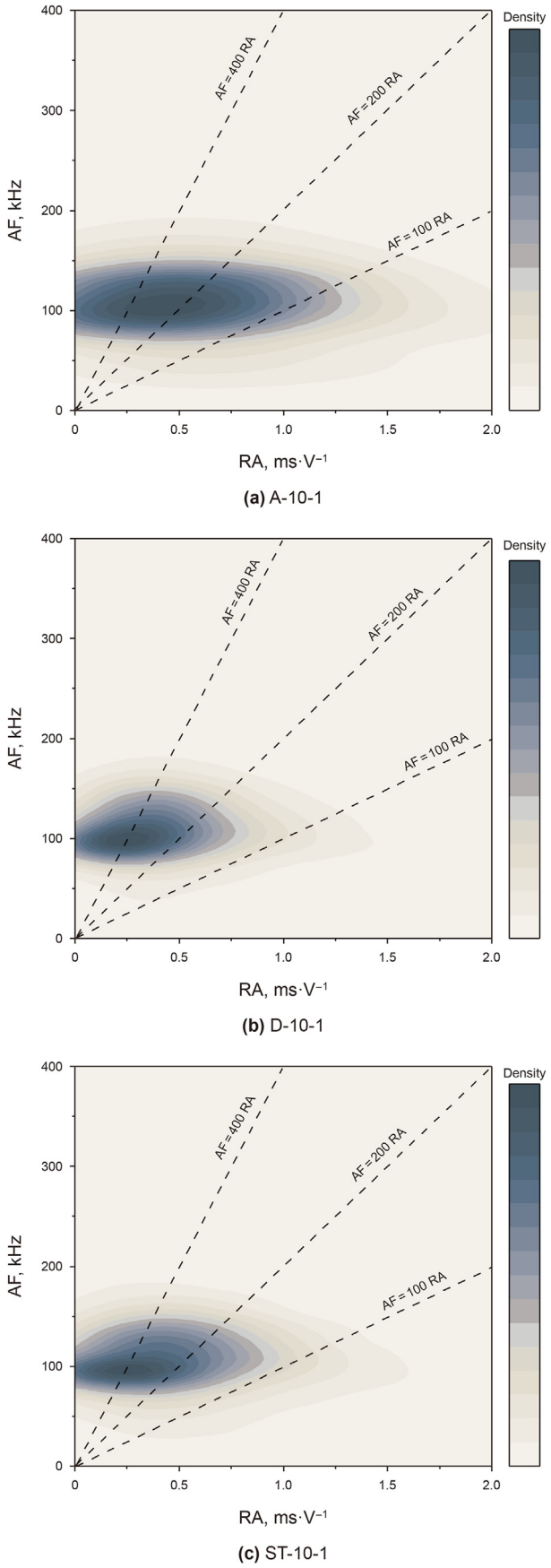

Fig. 14. RA-AF data density maps of typical samples (the blue area has higher data density and the gray area has lower data density).

Table 4
Crack percentages based on RA-AF method with different coefficients k.

σ_n, MPa	Bedding orientation	$k = 100$		$k = 200$		$k = 300$		$k = 400$		$k = 500$	
		Tensile, %	Shear, %	Tensile, %	Shear, %	Tensile, %	Shear, %	Tensile, %	Shear, %	Tensile, %	Shear, %
10	Arrester	83.98	16.02	66.16	33.84	46.63	53.37	31.99	68.01	23.57	76.43
	Divider	86.37	13.63	68.35	31.65	53.83	46.17	41.71	58.29	32.64	67.36
	Short-transverse	78.98	21.02	57.80	42.20	40.99	59.01	29.49	70.51	22.20	77.80
30	Arrester	78.85	21.15	57.68	42.32	41.07	58.93	29.93	70.07	22.76	77.24
	Divider	83.56	16.44	67.64	32.36	50.06	49.94	37.04	62.96	30.11	69.89
	Short-transverse	73.66	26.34	50.34	49.66	34.27	65.73	24.45	75.55	18.04	81.96
50	Arrester	73.45	26.55	52.34	47.66	37.38	62.62	27.42	72.58	21.09	78.91
	Divider	75.98	24.02	59.24	40.76	46.11	53.89	36.00	64.00	27.08	72.92
	Short-transverse	59.25	40.75	35.01	64.99	22.03	77.97	15.23	84.77	11.24	88.76

when entering the unstable cracking stage in the uniaxial compression test (Stanchits et al., 2006). According to Du et al. (2020), for different rock types, the percentage of shear cracks in the shear test is 66–72%. According to Table 4, AF = 400 RA was chosen as the reference transition line for further analysis.

The AE event locations at the peak shear stress of typical samples are shown in Fig. 15. Since thousands of AE events were observed for each sample, only the AE events with energy above 1000 aJ were plotted. The larger size and deeper color of the symbols indicate that more AE energy was released. The AE events were mainly located near the potential shear plane, and most high-energy AE events were caused by shear cracks. Tensile mode events were mainly located away from the shear plane, which might correspond to the propagation of the edge crack. Shear mode AE events were mainly located near the potential shear plane, demonstrating that the employed transition line was reasonable.

The shear crack percentage evolution during the crack coalescence stage under different normal stress conditions is shown in Fig. 16. When σ_n = 10 MPa, the shear crack percentage sharply increased when the shear stress reached the crack coalescence stress, which further indicated that the macrocrack generated at that time was shear-mode. Then, the shear crack percentage

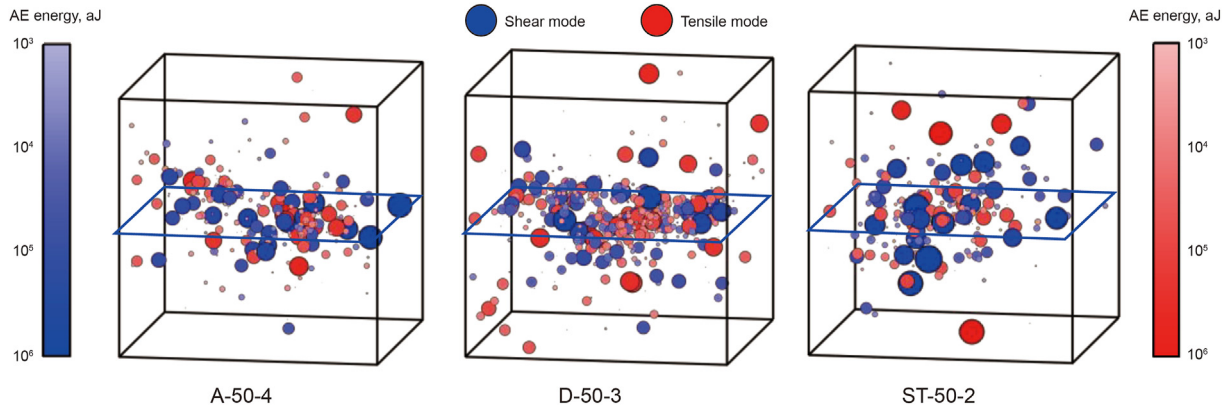

Fig. 15. Spatial distributions of AE events in typical samples at peak shear stress.

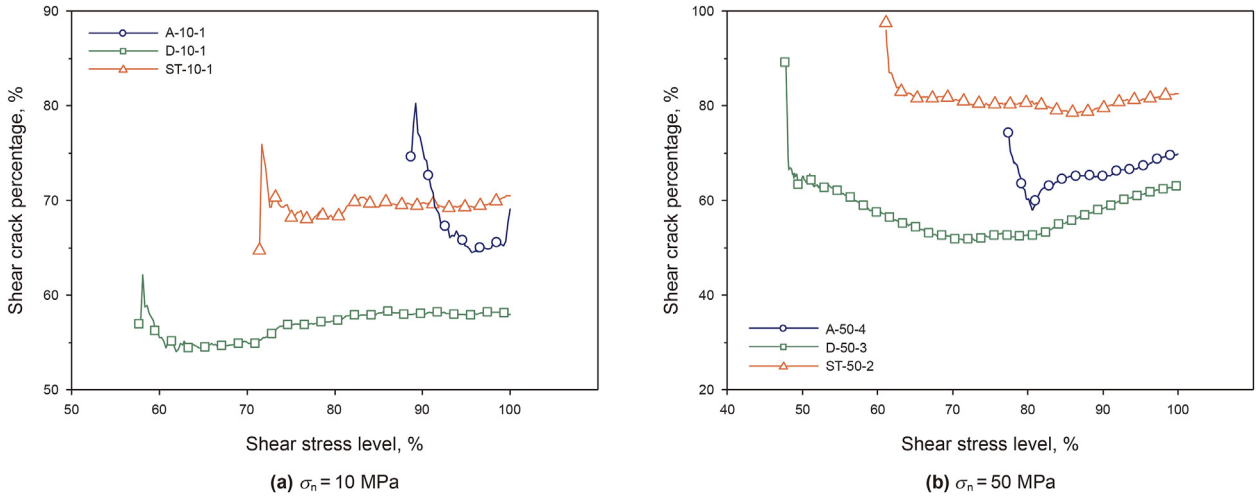

Fig. 16. Shear crack percentage evolution of typical samples during the crack coalescence stage (k = 400).

dramatically decreased, possibly because the macrocracks were continuously stretched under the effect of shear dilation. As the loading progressed, the shear crack percentage underwent a "concave" stage, i.e., the shear crack percentage first decreased and subsequently increased, indicating that the dominant microcracking mechanisms changed from tensile-mode to shear-mode. When $\sigma_n = 50$ MPa, the shear crack percentage sharply decreased once the shear stress reached the crack coalesce stress, and as analyzed above, two edge cracks were generated at that time. Accordingly, the edge cracks were likely classified into tensile-mode. Then, the shear crack percentage also underwent a gentle "concave" stage, and the shear crack percentage slowly increased. More importantly, high-energy AE events, with high ratios of AF/RA, occurred at the moment of final failure, demonstrating that the sample indeed failed by shear. In summary, the mechanisms of the progressive shear process were revealed. Before the crack coalescence stage, the microcracking was dominated by shear-mode. Once the shear stress reached the crack coalesce stress, macroscopic shear cracks occurred when $\sigma_n = 10$ MPa and macro tensile edge cracks occurred when $\sigma_n = 50$ MPa. Then, a transition of the failure mechanism from tension to shear was observed, resulting in the final macroscopic shear failure.

3.3. Anisotropy in the fracture network

3.3.1. 3D anisotropy in the fractal property of the fracture network

Fractures in a rock mass can significantly reduce its stability and increase the reservoir permeability (Ai et al., 2021; Dong et al., 2020; Ren et al., 2014; Zhang et al., 2021a, 2022), so the study on the anisotropic fracture network of shale after shearing is critically important. The 3D fracture network of each typical ruptured shale sample was obtained after processing and reconstruction of the 1700 scanning images using the system-provided pretreatment software Phoenix Datos|X 2 Rec, as shown in Fig. 17. The representative cross-sections of each typical ruptured sample are clearly displayed in Figs. 18–20, where the front and side view sections provide insight into the 2D fractures within the samples. A visual inspection shows that for a given normal stress level, the arrester and divider samples had much more complex fracture networks than the short-transverse sample. In addition, the generated fracture network was clearly sensitive to the applied normal stress for each bedding orientation. However, the differences in fracture networks were roughly determined by visual inspection, and a quantitative assessment is required to better understand the 3D anisotropy in the shear failure of shale.

As mentioned above, the generated fracture networks inside the ruptured samples were generally different for various bedding orientations and normal stress conditions. Therefore, the fractal geometry (Mandelbrot, 1982), which enables one to characterize the complexities and irregularities of an object, was adopted to archive a quantitative description of the generated fracture networks. Due to its simplicity and high accuracy, the cubic covering method in Ai et al. (2014); Zhou and Xie (2003) was employed to determine the fractal dimension (an indicator of the irregularity) of each fracture network. First, the spatial coordinate data with a 0.1 mm interval of the fracture network was extracted through programming. Then, the space (50 mm × 50 mm × 50 mm) was divided into many boxes with side length δ. The number of boxes required to cover the fracture network is $N(\delta)$. Different values of $N(\delta)$ can be obtained using different scales δ, and the fractal dimension can be calculated by

$$D = -\lim_{\delta \to 0} \frac{\ln N(\delta)}{\ln \delta} \tag{1}$$

where D is the fractal dimension of the fracture network and is mathematically obtained by the linear fitting of $\ln N(\delta)$ and $\ln \delta$.

In this work, six box scales δ (0.2, 0.5, 1.0, 2.0, 5.0 and 10.0 mm) were adopted to calculate the fractal dimension. The calculated fractal dimension was expected to vary from 2.0 to 3.0, and a higher value represented a more complex fracture network (Xie, 1996). The fractal dimension results are shown in Fig. 21. Under identical

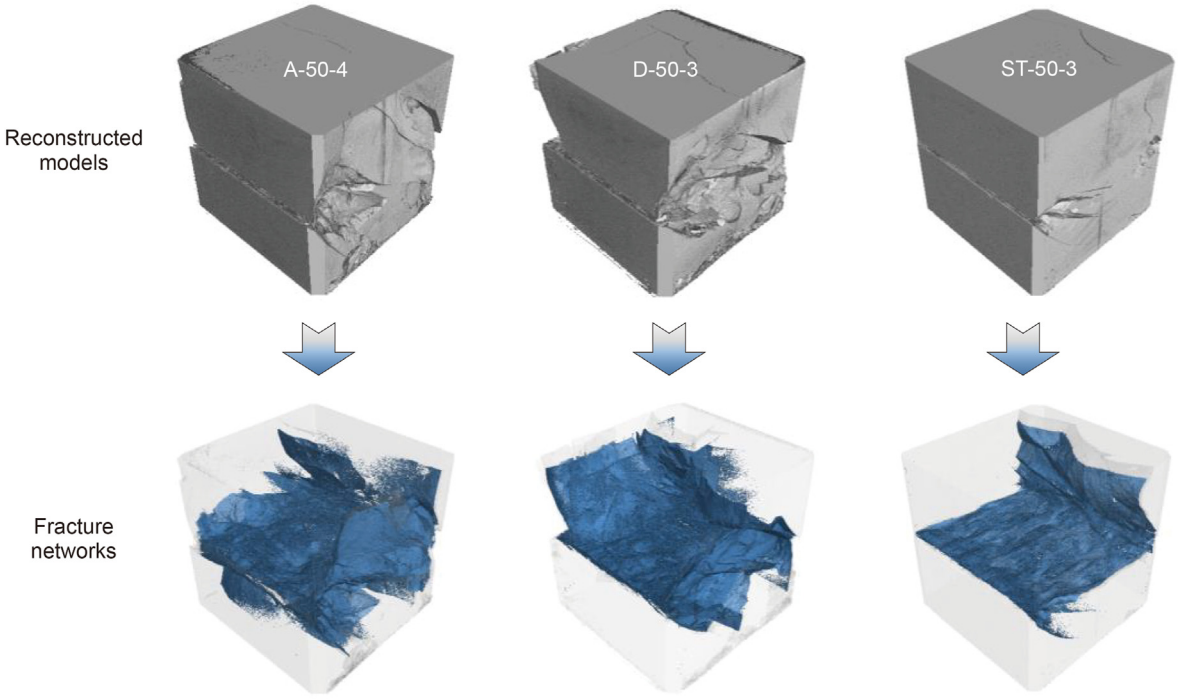

Fig. 17. Reconstructed models and fracture networks of typical samples.

normal stress conditions, the arrester sample has the largest fractal dimension, and the short-transverse sample has the smallest one. When σ_n = 10 MPa, the fractal dimension of the short-transverse sample was only 2.0327, indicating that its fracture network was almost a plane. In contrast, there were many tension-induced cracks in the front view sections of the arrester and divider samples. In addition, in the side view section of the divider sample, there were also many tensile cracks near the free surface even if σ_n = 10 MPa (see Fig. 19f). These results illustrated the short-transverse samples had the largest percentage of shear cracks and the divider samples had the smallest one. The occurrence of tensile cracks outside the shear band also increased the fractal dimension of the fracture network. Generally, the tensile cracks were restrained under high normal stress conditions, which has also been demonstrated in Section 3.2.2. In fact, only the tensile cracks perpendicular to the normal stress were restrained, while inclined, or even vertical, tensile cracks are not restrained but rather promoted. This phenomenon could be demonstrated in Figs. 18–20: when the normal stress increased, more tensile cracks were observed, especially in the side view sections. In addition, the failure under high normal stress conditions was extremely devastating. It can be inferred that the large-scale tensile cracks were generated due to the instantaneous release of strain energy when the final failure occurred. In summary, the 3D bedding orientation remarkably affected the dependency of the generated fracture networks under the applied normal stress, which had never been observed before.

3.3.2. 3D anisotropy in the fracture area and fracture volume

In addition to the complexity and irregularity of a fracture network, the fracture area and fracture volume of the fracture network are of concern in SRV treatment evaluation and well stability analysis and can provide additional information on the failure behavior of rocks. Therefore, an estimation of the fracture area and fracture volume of a ruptured shale sample can help examine the 3D anisotropy in the fracture network and differentiate the failure patterns. With the CT images, the fracture network was identified through the grayscale difference between rocks and fractures, and the fracture surface area A_f and fracture volume V_f were calculated using the VGStudio Max software. However, these area and volume parameters are scale-dependent and cannot accurately reflect the characteristics of a fracture network (Zhang et al., 2018). Therefore, the fracture density and intensity parameters of fracture networks P_{32} and FI defined in previous works (Lee et al., 2011; Zhang et al., 2015) were considered, i.e.,

$$\begin{cases} P_{32} = \dfrac{A_f}{V_v} \\ \mathrm{FI} = \dfrac{V_f}{V_v} \end{cases} \tag{2}$$

where V_v is the total volume of the rock matrix and fractures. Although P_{32} has a dimension, it is scale-independent and scale-invariant with respect to the fracture size distribution (Lee et al., 2011).

The fracture area, fracture volume, fracture density and fracture intensity of each typical ruptured sample are listed in Table 5. Clearly, the short-transverse samples always have the minimum P_{32} and FI under each normal stress condition. Therefore, when the shear direction is parallel to the bedding planes, it is not beneficial for generating complex fracture networks in shale reservoirs during hydraulic fracturing treatment. When σ_n = 10 MPa, the arrester sample had larger P_{32} and FI than the divider sample. When σ_n = 50 MPa, the arrester sample had a larger P_{32} and smaller FI. The divider sample had a larger fracture volume because the missing fragments were identified as fractures (see Fig. 19h). Therefore, a larger fracture area and fracture volume can be obtained with the arrester sample. In addition, the arrester sample had a smaller shear strength than the divide sample. This result may shed light on hydraulic fracturing, i.e., how to obtain a more complex fracture network with a lower cost.

Normally, microcrack initiation and propagation inside a rock sample are essentially driven by the input energy from the testing machine, i.e., the generation of a new fracture surface consumes energy. Therefore, more input energy is generally required to destroy a rock sample if a much larger fracture surface inside the sample is generated. To preliminarily verify the relationship between fracture surface area A_f and total input energy E_s, as listed in Table 5, the input energy for each ruptured sample was determined using the area enveloped by the load-displacement curve and the coordinate axis (Luo and Gong, 2020). As expected, fracture area A_f and input energy E_s have a strong linear relationship with a slope of 24,279 J m^{-2} (see Fig. 22). This result confirms that a larger strain

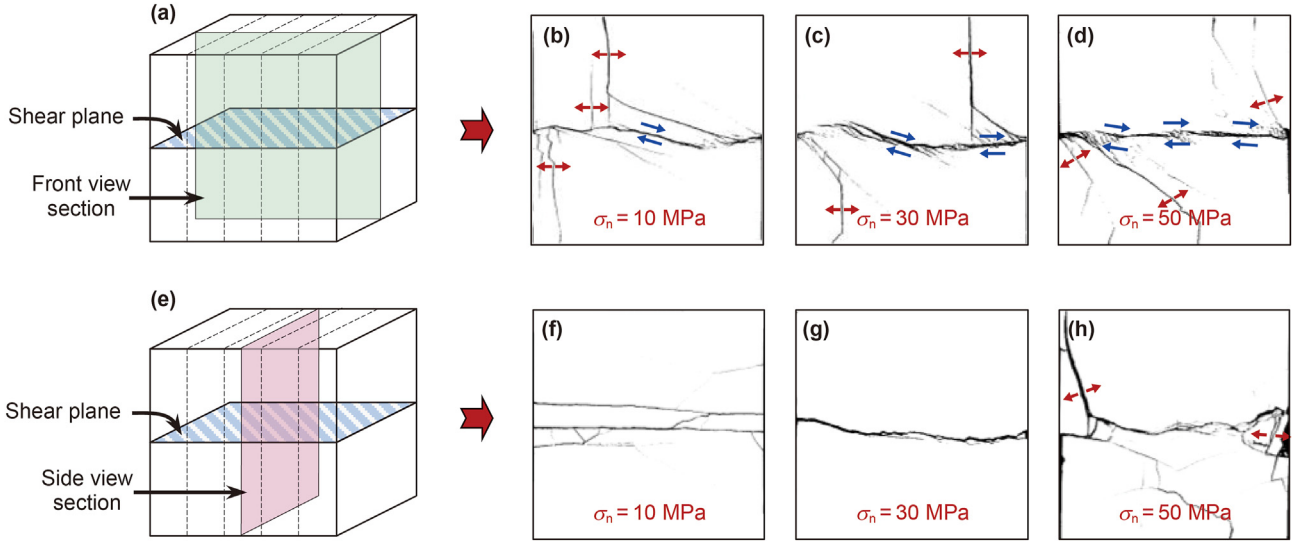

Fig. 18. Front view and side view sections of typical arrester samples (red arrows represent tensile cracks and blue arrows represent shear cracks).

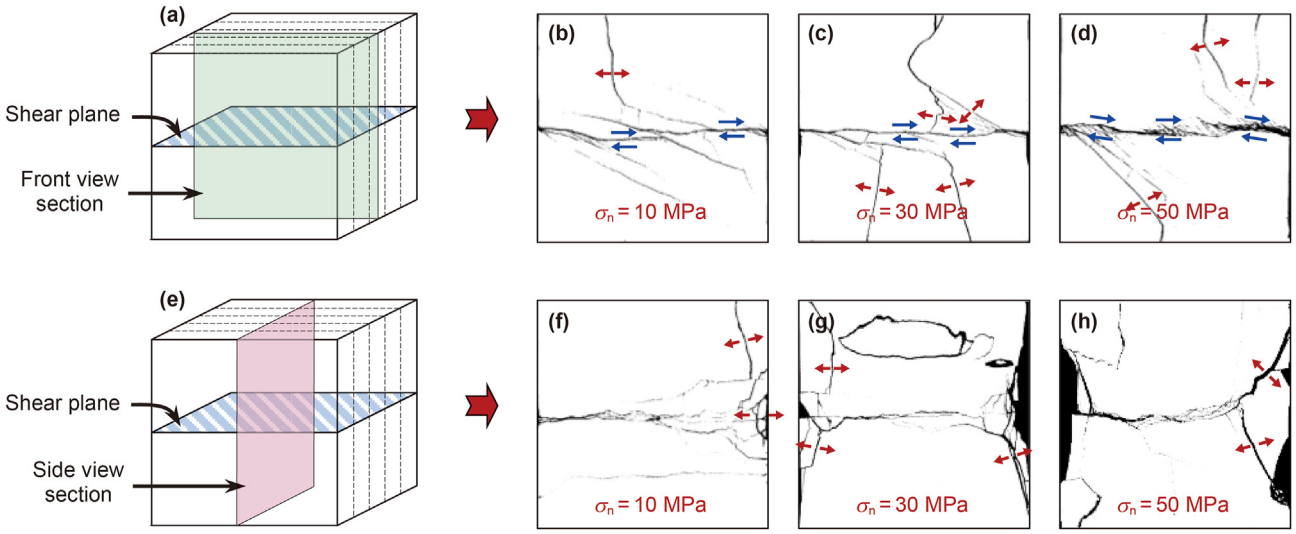

Fig. 19. Front view and side view sections of typical divider samples.

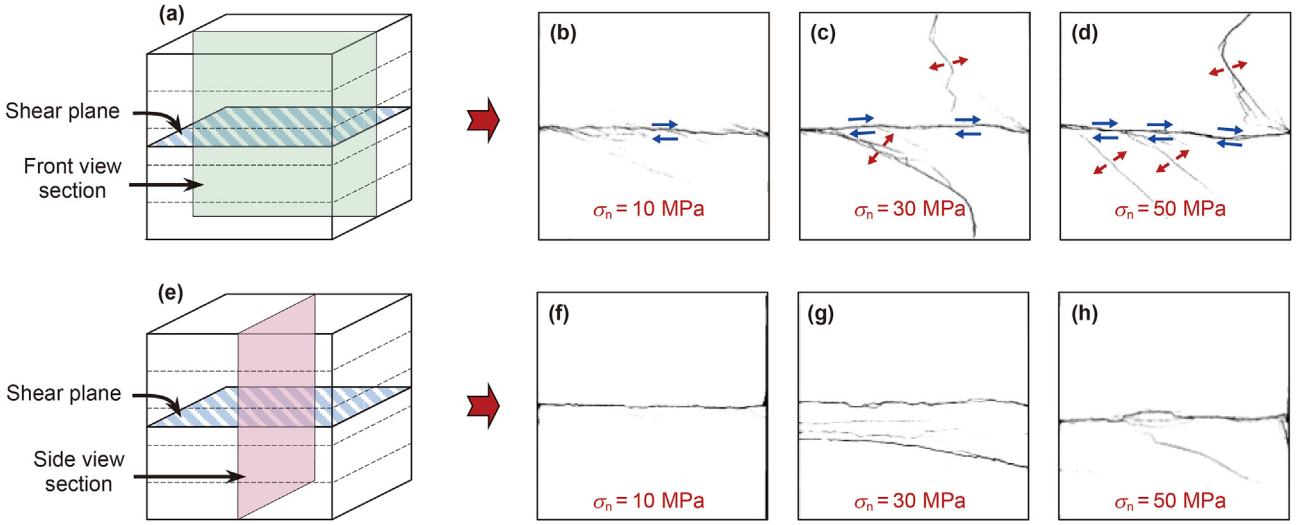

Fig. 20. Front view and side view sections of typical short-transverse samples.

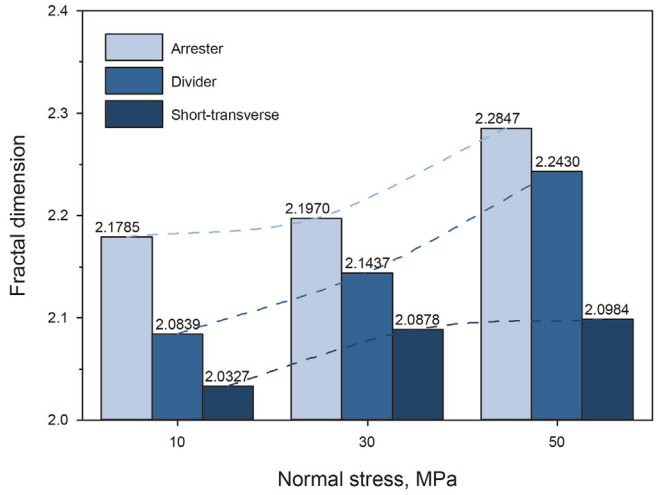

Fig. 21. The fractal dimensions of the 3D fracture networks.

Table 5
Characteristic parameters of the fracture network and strain energy of typical samples.

Sample no.	A_f, mm^2	V_f, mm^3	P_{32}	FI, %	E_s, J
A-10-1	32,577	1710	0.26	1.34	481.76
A-30-4	41,101	2896	0.32	2.26	887.57
A-50-4	67,389	5112	0.52	3.91	1406.19
D-10-1	30,575	1419	0.24	1.12	460.67
D-30-3	53,050	4115	0.41	3.16	1114.13
D-50-3	63,804	8872	0.47	6.60	1586.42
ST-10-1	16,154	833	0.13	0.66	305.73
ST-30-1	29,138	1569	0.23	1.24	816.19
ST-50-3	42,750	2005	0.34	1.60	1092.35

energy is required to generate more fracture surfaces, ultimately resulting in a higher peak shear strength, i.e., the anisotropy in the peak shear strength coincides with the anisotropy in the fracture surface area.

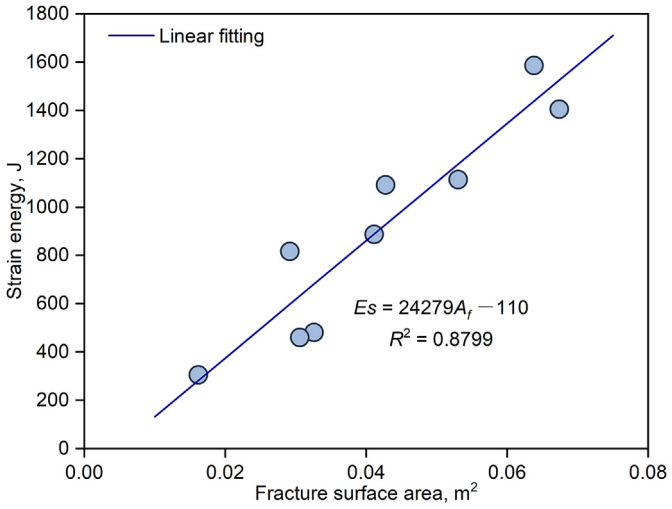

Fig. 22. Relationship between the strain energy and fracture surface area.

4. Conclusions

In this paper, a series of direct shear tests on cubic samples of Longmaxi shale with three typical bedding angles (i.e., arrester, divider and short-transverse orientations) were conducted. The 3D anisotropies in the shear strength parameters and failure behaviors were comprehensively investigated and highlighted. The following conclusions were presented based on these studies:

(1) The shear parameters of Longmaxi shale exhibited significant 3D anisotropies. The peak shear strength, cohesion and internal friction angle of the divider samples should be considered equal to those of the shale matrix, which are larger than those of the arrester samples.
(2) Combining the AE and DIC techniques, four characteristic stress levels were identified for the studied shale: the elastic deformation initiation, crack initiation, crack coalescence and peak stress thresholds, and the onset and accelerated development of shear damage-induced dilation were observed at the crack initiation and coalescence stress thresholds, respectively.
(3) At the crack coalescence stress threshold, a macroscopic shear crack was first generated near the potential shear plane under the low normal stress condition, while macroscopic tensile edge cracks first initiated from the two ends of the potential shear plane under the high normal stress condition. During the crack coalescence stage, the dominant micro-cracking mechanism changed from tensile-mode to shear-mode.
(4) Under identical applied normal stress conditions, more tensile cracks were generated when the bedding planes were perpendicular to the shear plane. Compared with the divider samples, a more complex fracture network with a larger fracture area and volume was obtained in the arrester samples, whose strengths were smaller.

Declaration of competing interest

The authors declare that they have no known competing financial interests or personal relationships that could have appeared to influence the work reported in this paper.

Acknowledgments

This research was funded by the National Natural Science Foundation of China (No. 12172240 and No. 51704198) and Department of Science and Technology of Sichuan Province (No. 2021YFH0030).

References

Aggelis, D.G., 2011. Classification of cracking mode in concrete by acoustic emission parameters. Mech. Res. Commun. 38 (3), 153–157. https://doi.org/10.1016/j.mechrescom.2011.03.007.
Ai, T., Wu, S., Zhang, R., et al., 2021. Changes in the structure and mechanical properties of a typical coal induced by water immersion. Int. J. Rock Mech. Min. Sci. 138. https://doi.org/10.1016/j.ijrmms.2020.104597.
Ai, T., Zhang, R., Zhou, H.W., et al., 2014. Box-counting methods to directly estimate the fractal dimension of a rock surface. Appl. Surf. Sci. 314, 610–621. https://doi.org/10.1016/j.apsusc.2014.06.152.
Arthur, J.D., Bohm, B., Layne, M., 2009. Hydraulic fracturing considerations for natural gas wells of the Marcellus Shale. Gulf Coast Association of Geological Societies Transactions 59, 49–59.
Asaka, M., Holt, R.M., 2020. Anisotropic wellbore stability analysis: impact on failure prediction. Rock Mech. Rock Eng. 54 (2), 583–605. https://doi.org/10.1007/s00603-020-02283-0.
Backers, T., Gruehser, C., Meier, T., et al., 2012. Fracture Pattern of Borehole Breakouts in Shale - Comparison of Physical and Numerical Experiments. https://doi.org/10.3997/2214-4609.20148137.
Carey, J.W., Lei, Z., Rougier, E., et al., 2015. Fracture-permeability behavior of shale. J. Unconv. Oil Gas Resour. 11, 27–43. https://doi.org/10.1016/j.juogr.2015.04.003.
Chen, B., Barboza, B.R., Sun, Y., et al., 2021a. A review of hydraulic fracturing simulation. Arch. Comput. Methods Eng. https://doi.org/10.1007/s11831-021-09653-z.
Chen, H., Di, Q., Zhang, W., et al., 2021b. Effects of bedding orientation on the failure pattern and acoustic emission activity of shale under uniaxial compression. Geomech. Geophys. Geo-Energy Geo-Resour. 7 (1). https://doi.org/10.1007/s40948-021-00216-x.
Cho, J.W., Kim, H., Jeon, S., et al., 2012. Deformation and strength anisotropy of Asan gneiss, Boryeong shale, and Yeoncheon schist. Int. J. Rock Mech. Min. Sci. 50, 158–169. https://doi.org/10.1016/j.ijrmms.2011.12.004.
Chong, K.P., Kuruppu, M.D., Kuszmaul, J.S., 1987. Fracture-toughness determination of layered materials. Eng. Fract. Mech. 28 (1), 43–54. https://doi.org/10.1016/0013-7944(87)90118-4.
Ding, C., Zhang, Y., Hu, D., et al., 2021. Correction to: foliation effects on mechanical and failure characteristics of slate in 3D space under Brazilian test conditions. Rock Mech. Rock Eng. 54 (11), 5963. https://doi.org/10.1007/s00603-021-02460-9.
Dixon, W.J., 1950. Analysis of extreme values. Ann. Math. Stat. 21 (4), 488–506.
Dong, Y., Zhu, Z., Ren, L., et al., 2020. Crack dynamic propagation properties and arrest mechanism under impact loading. J. Rock Mech. Geotech. Eng. 12 (6), 1171–1184. https://doi.org/10.1016/j.jrmge.2020.01.008.
Du, K., Li, X., Tao, M., et al., 2020. Experimental study on acoustic emission (AE) characteristics and crack classification during rock fracture in several basic lab tests. Int. J. Rock Mech. Min. Sci. 133. https://doi.org/10.1016/j.ijrmms.2020.104411.
Fan, Z.D., Xie, H.P., Ren, L., et al., 2022a. Anisotropy in shear-sliding fracture behavior of layered shale under different normal stress conditions. J. Cent. South Univ. https://doi.org/10.1007/s11771-022-5156-9.
Fan, Z.D., Xie, H.P., Zhang, R., et al., 2022b. Characterization of anisotropic mode II fracture behaviors of a typical layered rock combining AE and DIC techniques. Eng. Fract. Mech. 271. https://doi.org/10.1016/j.engfracmech.2022.108599.
Frash, L.P., Carey, J.W., Lei, Z., et al., 2016. High-stress triaxial direct-shear fracturing of Utica shale and in situ X-ray microtomography with permeability measurement. J. Geophys. Res. Solid Earth 121 (7), 5493–5508. https://doi.org/10.1002/2016jb012850.
He, R., He, L., Guan, B., et al., 2021. Mechanical properties of a typical Jurassic Shaximiao sandstone under Subzero and deep in situ temperature conditions. Front. Earth Sci. 9. https://doi.org/10.3389/feart.2021.770272.
He, R., Ren, L., Zhang, R., et al., 2022. Anisotropy characterization of the elasticity and energy flow of Longmaxi shale under uniaxial compression. Energy Rep. 8, 1410–1424. https://doi.org/10.1016/j.egyr.2021.12.050.
Heng, S., Guo, Y.T., Yang, C.H., et al., 2015. Experimental and theoretical study of the anisotropic properties of shale. Int. J. Rock Mech. Min. Sci. 74, 58–68. https://doi.org/10.1016/j.ijrmms.2015.01.003.
Heng, S., Li, X., Liu, X., et al., 2020. Experimental study on the mechanical properties of bedding planes in shale. J. Nat. Gas Sci. Eng. 76. https://doi.org/10.1016/j.jngse.2020.103161.
Hou, P., Gao, F., Yang, Y.G., et al., 2016. Effect of the layer orientation on mechanics and energy evolution characteristics of shales under uniaxial loading. Int. J. Min. Sci. Technol. 26 (5), 857–862. https://doi.org/10.1016/j.ijmst.2016.05.041.
Huang, B., Li, L., Tan, Y., et al., 2020. Investigating the meso-mechanical anisotropy and fracture surface roughness of continental shale. J. Geophys. Res. Solid Earth 125 (8). https://doi.org/10.1029/2019jb017828.

Jaeger, J.C., Cook, N.G., Zimmerman, R., 2009. Fundamentals of Rock Mechanics. John Wiley & Sons, New Jersey.
Jin, Z.F., Li, W.X., Jin, C.R., et al., 2018. Anisotropic elastic, strength, and fracture properties of Marcellus shale. Int. J. Rock Mech. Min. Sci. 109, 124–137. https://doi.org/10.1016/j.ijrmms.2018.06.009.
Keneti, S.A.R., Wong, R.C.K., 2011. Shear behavior of the Montney shale under double-shear test. In: 45th U.S. Rock Mechanics/Geomechanics Symposium. ARMA-11-277.
Kirsch, C., 1898. Die theorie der elastizitat und die bedurfnisse der festigkeitslehre. Z. Des. Vereines Dtsch. Ingenieure 42, 797–807.
Lee, C.C., Lee, C.H., Yeh, H.F., et al., 2011. Modeling spatial fracture intensity as a control on flow in fractured rock. Environ. Earth Sci. 63 (6), 1199–1211. https://doi.org/10.1007/s12665-010-0794-x.
Lei, R.D., Zhang, Z.Y., Berto, F., et al., 2020. Cracking process and acoustic emission characteristics of sandstone with two parallel filled-flaws under biaxial compression. Eng. Fract. Mech. 237, 107253. https://doi.org/10.1016/j.engfracmech.2020.107253.
Li, C.B., Xie, H.P., Wang, J., 2020. Anisotropic characteristics of crack initiation and crack damage thresholds for shale. Int. J. Rock Mech. Min. Sci. 126, 104178. https://doi.org/10.1016/j.ijrmms.2019.104178.
Li, L.C., Tang, C.A., Li, G., et al., 2012. Numerical simulation of 3D hydraulic fracturing based on an improved flow-stress-damage model and a parallel FEM technique. Rock Mech. Rock Eng. https://doi.org/10.1007/s00603-012-0252-z.
Li, W.X., Rezakhani, R., Jin, C.R., et al., 2017. A multiscale framework for the simulation of the anisotropic mechanical behavior of shale. Int. J. Numer. Anal. Methods GeoMech. 41 (14), 1494–1522. https://doi.org/10.1002/nag.2684.
Lin, Q., Wang, S.Q., Wan, B., et al., 2020. Characterization of fracture process in sandstone: a linear correspondence between acoustic emission energy density and opening displacement gradient. Rock Mech. Rock Eng. 53 (2), 975–981. https://doi.org/10.1007/s00603-019-01949-8.
Lu, H., Zhang, R., Ren, L., et al., 2021a. Damage characterization of shale under uniaxial compression by acoustic emission monitoring. Front. Earth Sci. https://doi.org/10.1007/s11707-021-0911-z.
Lu, H.J., Xie, H.P., Luo, Y., et al., 2021b. Failure characterization of Longmaxi shale under direct shear mode loadings. Int. J. Rock Mech. Min. Sci. 148, 104936. https://doi.org/10.1016/j.ijrmms.2021.104936.
Luo, S., Gong, F.Q., 2020. Linear energy storage and dissipation laws of rocks under preset angle shear conditions. Rock Mech. Rock Eng. 53 (7), 3303–3323. https://doi.org/10.1007/s00603-020-02105-3.
Ma, T., Qiu, Y., Liu, D., et al., 2020. Shear strength parameter determination for the single plane of weakness criterion: implications for wellbore stability. IOP Conf. Ser. Earth Environ. Sci. 570 (3). https://doi.org/10.1088/1755-1315/570/3/032008.
Mandelbrot, B.B., 1982. The Fractal Geometry of Nature. WH freeman, New York.
Masri, M., Sibai, M., Shao, J.F., et al., 2014. Experimental investigation of the effect of temperature on the mechanical behavior of Tournemire shale. Int. J. Rock Mech. Min. Sci. 70, 185–191. https://doi.org/10.1016/j.ijrmms.2014.05.007.
McClure, M., Horne, R., 2014. Characterizing hydraulic fracturing with a tendency-for-shear-stimulation test. SPE Reservoir Eval. Eng. 17 (2), 233–243. https://doi.org/10.2118/166332-MS.
Miao, S.T., Pan, P.Z., Zhao, X.G., et al., 2021. Experimental study on damage and fracture characteristics of Beishan granite subjected to high-temperature treatment with DIC and AE techniques. Rock Mech. Rock Eng. 54 (2), 721–743. https://doi.org/10.1007/s00603-020-02271-4.
Moradian, Z.A., Ballivy, G., Rivard, P., et al., 2010. Evaluating damage during shear tests of rock joints using acoustic emissions. Int. J. Rock Mech. Min. Sci. 47 (4), 590–598. https://doi.org/10.1016/j.ijrmms.2010.01.004.
Niandou, H., Shao, J.F., Henry, J.P., et al., 1997. Laboratory investigation of the mechanical behaviour of Tournemire shale. Int. J. Rock Mech. Min. Sci. 34 (1), 3–16. https://doi.org/10.1016/s1365-1609(97)80029-9.
Ohno, K., Ohtsu, M., 2010. Crack classification in concrete based on acoustic emission. Construct. Build. Mater. 24 (12), 2339–2346. https://doi.org/10.1016/j.conbuildmat.2010.05.004.
Palmer, I.D., Moschovidis, Z.A., Cameron, J.R., 2007. Modeling shear failure and stimulation of the Barnett shale after hydraulic fracturing. In: SPE Hydraulic Fracturing Technology Conference. https://doi.org/10.2118/106113-ms. SPE-106113-MS.
Ren, L., Xie, H.P., Sun, X., et al., 2020. Characterization of anisotropic fracture properties of Silurian Longmaxi shale. Rock Mech. Rock Eng. 54 (2), 665–678. https://doi.org/10.1007/s00603-020-02288-9.
Ren, L., Zhu, Z., Wang, M., et al., 2014. Mixed-mode elastic-plastic fractures: improved R-criterion. J. Eng. Mech. 140 (6). https://doi.org/10.1061/(asce)em.1943-7889.0000755.
Saiang, D., Malmgren, L., Nordlund, E., 2005. Laboratory tests on shotcrete-rock joints in direct shear, tension and compression. Rock Mech. Rock Eng. 38 (4), 275–297. https://doi.org/10.1007/s00603-005-0055-6.
Shen, P., Tang, H., Zhang, B., et al., 2021. Weakening investigation of reservoir rock by coupled uniaxial compression, computed tomography and digital image correlation methods: a case study. Sensors 21 (2), 344. https://doi.org/10.3390/s21020344.
Stanchits, S., Vinciguerra, S., Dresen, G., 2006. Ultrasonic velocities, acoustic emission characteristics and crack damage of basalt and granite. Pure Appl. Geophys. 163 (5–6), 975–994. https://doi.org/10.1007/s00024-006-0059-5.
Suo, Y., Chen, Z.X., Rahman, S.S., et al., 2020. Experimental study on mechanical and anisotropic properties of shale and estimation of uniaxial compressive strength. Energy Sources, Part A Recovery, Util. Environ. Eff. 1–11. https://doi.org/10.1080/15567036.2020.1779873.
Wang, M.M., Li, P., Wu, X.W., et al., 2016. A study on the brittleness and progressive failure process of anisotropic shale. Environ. Earth Sci. 75 (10), 886. https://doi.org/10.1007/s12665-016-5700-8.
Wang, Y., Li, C.H., 2017. Investigation of the P- and S-wave velocity anisotropy of a Longmaxi formation shale by real-time ultrasonic and mechanical experiments under uniaxial deformation. J. Petrol. Sci. Eng. 158, 253–267. https://doi.org/10.1016/j.petrol.2017.08.054.
Wu, Y., Li, X., He, J., et al., 2016. Mechanical properties of Longmaxi black organic-rich shale samples from South China under uniaxial and triaxial compression states. Energies 9 (12). https://doi.org/10.3390/en9121088.
Xie, H.P., 1996. Fractal in Rock Mechanics. Science Press, Beijing (in Chinese).
Yan, C.L., Deng, J.G., Cheng, Y.F., et al., 2017. Mechanical properties of gas shale during drilling operations. Rock Mech. Rock Eng. 50 (7), 1753–1765. https://doi.org/10.1007/s00603-017-1203-5.
Yang, S.Q., Yin, P.F., Li, B., et al., 2020. Behavior of transversely isotropic shale observed in triaxial tests and Brazilian disc tests. Int. J. Rock Mech. Min. Sci. 133, 104435. https://doi.org/10.1016/j.ijrmms.2020.104435.
Zhang, A., Xie, H., Zhang, R., et al., 2021a. Dynamic failure behavior of Jinping marble under various preloading conditions corresponding to different depths. Int. J. Rock Mech. Min. Sci. 148. https://doi.org/10.1016/j.ijrmms.2021.104959.
Zhang, A.L., Zhang, R., Gao, M.Z., et al., 2020a. Failure behavior and damage characteristics of coal at different depths under triaxial unloading based on acoustic emission. Energies 13 (17), 4451. https://doi.org/10.3390/en13174451.
Zhang, J.Z., Zhou, X.P., Zhou, L.S., et al., 2019. Progressive failure of brittle rocks with non-isometric flaws: insights from acousto-optic-mechanical (AOM) data. Fatig. Fract. Eng. Mater. Struct. 42 (8), 1787–1802. https://doi.org/10.1111/ffe.13019.
Zhang, R., Ai, T., Ren, L., et al., 2018. Failure characterization of three typical coal-bearing formation rocks using acoustic emission monitoring and X-ray computed tomography techniques. Rock Mech. Rock Eng. 52 (6), 1945–1958. https://doi.org/10.1007/s00603-018-1677-9.
Zhang, R., Ai, T., Zhou, H.W., et al., 2015. Fractal and volume characteristics of 3D mining-induced fractures under typical mining layouts. Environ. Earth Sci. 73 (10), 6069–6080. https://doi.org/10.1007/s12665-015-4376-9.
Zhang, R., Xie, H.P., Ren, L., et al., 2022. Excavation-induced structural deterioration of rock masses at different depths. Arch. Civ. Mech. Eng. 22 (2). https://doi.org/10.1007/s43452-022-00401-z.
Zhang, Y., Jiang, Y., Asahina, D., et al., 2021b. Structural effect of en-echelon fractures on shear behavior of rock mass under constant normal load conditions: an experimental study. Rock Mech. Rock Eng. 54 (9), 4825–4849. https://doi.org/10.1007/s00603-021-02555-3.
Zhang, Z.-H., Deng, J.-H., 2020. A new method for determining the crack classification criterion in acoustic emission parameter analysis. Int. J. Rock Mech. Min. Sci. 130. https://doi.org/10.1016/j.ijrmms.2020.104323.
Zhang, Z.T., Xie, H.P., Zhang, R., et al., 2020b. Size and spatial fractal distributions of coal fracture networks under different mining-induced stress conditions. Int. J. Rock Mech. Min. Sci. 132, 104364. https://doi.org/10.1016/j.ijrmms.2020.104364.
Zhao, X.G., Cai, M., 2010. A mobilized dilation angle model for rocks. Int. J. Rock Mech. Min. Sci. 47 (3), 368–384. https://doi.org/10.1016/j.ijrmms.2009.12.007.
Zhao, X.G., Cai, M., Wang, J., et al., 2015. Objective determination of crack initiation stress of brittle rocks under compression using AE measurement. Rock Mech. Rock Eng. 48 (6), 2473–2484. https://doi.org/10.1007/s00603-014-0703-9.
Zheng, L., Wang, L., Zhu, L., et al., 2021. Analytical model of the shear behaviors of bolted rough joints based on the dilation effect and surface abrasion. Eng. Geol. 294. https://doi.org/10.1016/j.enggeo.2021.106399.
Zhou, H.W., Xie, H., 2003. Direct estimation of the fractal dimensions of a fracture surface of rock. Surf. Rev. Lett. 10 (5), 751–762. https://doi.org/10.1142/S0218625X03005591.
Zhu, J., Deng, J., Chen, F., et al., 2022. Failure analysis of water-bearing rock under direct tension using acoustic emission. Eng. Geol. 299. https://doi.org/10.1016/j.enggeo.2022.106541.
Zhu, Q.Q., Li, D.Y., Han, Z.Y., et al., 2019. Mechanical properties and fracture evolution of sandstone specimens containing different inclusions under uniaxial compression. Int. J. Rock Mech. Min. Sci. 115, 33–47. https://doi.org/10.1016/j.ijrmms.2019.01.010.